

SILVERRUSH. II. First Catalogs and Properties of $\sim 2,000$ $\text{Ly}\alpha$ Emitters and Blobs at $z \sim 6 - 7$ Identified over the $14 - 21 \text{ deg}^2$ Sky

Takatoshi Shibuya¹, Masami Ouchi^{1,2}, Akira Konno^{1,3}, Ryo Higuchi^{1,4},
Yuichi Harikane^{1,4}, Yoshiaki Ono¹, Kazuhiro Shimasaku^{3,5}, Yoshiaki
Taniguchi⁶, Masakazu A. R. Kobayashi⁷, Masaru Kajisawa⁸, Tohru
Nagao⁸, Hisanori Furusawa⁹, Tomotsugu Goto¹⁰, Nobunari Kashikawa^{9,11},
Yutaka Komiyama^{9,11}, Haruka Kusakabe³, Chien-Hsiu Lee¹², Rieko
Momose¹⁰, Kimihiko Nakajima¹³, Masayuki Tanaka^{9,11}, Shiang-Yu Wang¹⁴,
and Suraphong Yuma¹⁵

¹Institute for Cosmic Ray Research, The University of Tokyo, 5-1-5 Kashiwanoha, Kashiwa, Chiba 277-8582, Japan

²Kavli Institute for the Physics and Mathematics of the Universe (Kavli IPMU, WPI), University of Tokyo, Kashiwa, Chiba 277-8583, Japan

³Department of Astronomy, Graduate School of Science, The University of Tokyo, 7-3-1 Hongo, Bunkyo, Tokyo 113-0033, Japan

⁴Department of Physics, Graduate School of Science, The University of Tokyo, 7-3-1 Hongo, Bunkyo, Tokyo 113-0033, Japan

⁵Research Center for the Early Universe, Graduate School of Science, The University of Tokyo, 7-3-1 Hongo, Bunkyo, Tokyo 113-0033, Japan

⁶The Open University of Japan, Wakaba 2-11, Mihama-ku, Chiba 261-8586, Japan

⁷Faculty of Natural Sciences, National Institute of Technology, Kure College, 2-2-11 Agaminami, Kure, Hiroshima 737-8506, Japan

⁸Research Center for Space and Cosmic Evolution, Ehime University, Bunkyo-cho 2-5, Matsuyama 790-8577, Japan

⁹National Astronomical Observatory, Mitaka, Tokyo 181-8588, Japan

¹⁰Institute of Astronomy, National Tsing Hua University, 101 Section 2, Kuang-Fu Road, Hsinchu 30013, Taiwan

¹¹The Graduate University for Advanced Studies (SOKENDAI), 2-21-1 Osawa, Mitaka, Tokyo 181-8588

¹²Subaru Telescope, NAOJ, 650 N Aohoku Pl., Hilo, HI 96720, USA

¹³European Southern Observatory, Karl-Schwarzschild-Str. 2, D-85748, Garching bei Munchen, Germany

¹⁴Academia Sinica, Institute of Astronomy and Astrophysics, 11F of AS/NTU Astronomy-Mathematics Building, No.1, Sec. 4, Roosevelt Rd, Taipei 10617, Taiwan

¹⁵Department of Physics, Faculty of Science, Mahidol University, Bangkok 10400, Thailand

[‡]Based on data obtained with the Subaru Telescope. The Subaru Telescope is operated by

the National Astronomical Observatory of Japan.

*E-mail: shibyat@icrr.u-tokyo.ac.jp

Received (reception date); Accepted (acceptation date)

Abstract

We present an unprecedentedly large catalog consisting of 2,230 $\gtrsim L^*$ Ly α emitters (LAEs) at $z = 5.7$ and 6.6 on the 13.8 and 21.2 deg² sky, respectively, that are identified by the SILVERRUSH program with the first narrowband imaging data of the Hyper Suprime-Cam (HSC) survey. We confirm that the LAE catalog is reliable on the basis of 96 LAEs whose spectroscopic redshifts are already determined by this program and the previous studies. This catalogue is also available on-line. Based on this catalogue, we derive the rest-frame Ly α equivalent-width distributions of LAEs at $z \simeq 5.7 - 6.6$ that are reasonably explained by the exponential profiles with the scale lengths of $\simeq 120 - 170 \text{ \AA}$, showing no significant evolution from $z \simeq 5.7$ to $z \simeq 6.6$. We find that 275 LAEs with a large equivalent width (LEW) of $> 240 \text{ \AA}$ are candidates of young-metal poor galaxies and AGNs. We also find that the fraction of LEW LAEs to all ones is 4% and 21% at $z \simeq 5.7$ and $z \simeq 6.6$, respectively. Our LAE catalog includes 11 Ly α blobs (LABs) that are LAEs with spatially extended Ly α emission whose profile is clearly distinguished from those of stellar objects at the $\gtrsim 3\sigma$ level. The number density of the LABs at $z = 6 - 7$ is $\sim 10^{-7} - 10^{-6} \text{ Mpc}^{-3}$, being $\sim 10 - 100$ times lower than those claimed for LABs at $z \simeq 2 - 3$, suggestive of disappearing LABs at $z \gtrsim 6$, albeit with the different selection methods and criteria for the low and high- z LABs.

Key words: early universe — galaxies: formation — galaxies: high-redshift

1 Introduction

Ly α Emitters (LAEs) are one of important populations of high- z star-forming galaxies in the paradigm of the galaxy formation and evolution. Such galaxies are thought to be typically young (an order of 100 Myr; e.g., Finkelstein et al. 2007; Gawiser et al. 2007; Finkelstein et al. 2007), compact (an effective radius of $< 1 \text{ kpc}$; e.g., Taniguchi et al. 2009; Bond et al. 2012), less-massive (a stellar mass of $10^8 - 10^9 M_\odot$; e.g., Ono et al. 2010; Guaita et al. 2011), metal-poor ($\simeq 0.1$ of the solar metallicity; e.g., Nakajima et al. 2012; Nakajima et al. 2013; Nakajima & Ouchi 2014; Kojima et al. 2016), less-dusty than Lyman break galaxies (e.g., Blanc et al. 2011; Kusakabe et al. 2015), and a possible progenitor of Milky Way mass galaxies (e.g., Dressler et al. 2011). In addition, LAEs are used to probe the cosmic reionization, because ionizing photons escaped from a large number of massive stars formed in LAEs contribute to the ionization of intergalactic medium (IGM; e.g., Rhoads & Malhotra 2001; Malhotra & Rhoads 2006; Shimasaku et al. 2006; Kashikawa et al. 2006; Ouchi et al. 2008; Ouchi et al. 2010; Cowie et al. 2010; Hu et al. 2010; Kashikawa et al. 2011; Shibuya et al. 2012; Konno et al. 2014; Matthee et al. 2015; Matthee et al. 2015; Ota et al. 2017; Zheng et al. 2017).

LAEs have been surveyed by imaging observations with dedicated narrow-band (NB) filters for a prominent redshifted

Ly α emission (e.g., Ajiki et al. 2002; Malhotra & Rhoads 2004; Kodaira et al. 2003; Taniguchi et al. 2005; Gronwall et al. 2007; Erb et al. 2011; Ciardullo et al. 2012). In large LAE sample constructed by the NB observations, two rare Ly α -emitting populations have been identified: large equivalent width (LEW) LAEs, and spatially extended Ly α LAEs, Ly α blobs (LABs).

LEW LAEs are objects with a large Ly α equivalent width (EW) of $\gtrsim 240 \text{ \AA}$ which are not reproduced with the normal Salpeter stellar initial mass function (e.g., Malhotra & Rhoads 2002). Such an LEW is expected to be originated from complicated physical processes such as (i) photoionization by young and/or low-metallicity star-formation, (ii) photoionization by active galactic nucleus (AGN), (iii) photoionization by external UV sources (QSO fluorescence), (iv) collisional excitation due to strong outflows (shock heating), (v) collisional excitation due to gas inflows (gravitational cooling), and (vi) clumpy ISM (see e.g., Hashimoto et al. 2017). The highly-complex radiative transfer of Ly α in the interstellar medium (ISM) makes it difficult to understand the Ly α emitting mechanism (Neufeld 1991; Hansen & Oh 2006; Finkelstein et al. 2008; Laursen et al. 2013; Laursen et al. 2009; Laursen & Sommer-Larsen 2007; Zheng et al. 2010; Yajima et al. 2012; Duval et al. 2013; Zheng & Wallace 2013).

LABs are spatially extended Ly α gaseous nebulae in the high- z Universe (e.g., Steidel et al. 2000; Matsuda et al.

2004; Prescott et al. 2009; Matsuda et al. 2009; Matsuda et al. 2011; Prescott et al. 2012a; Prescott et al. 2012b; Prescott et al. 2013; Cantalupo et al. 2014; Arrigoni Battaia et al. 2015b; Hennawi et al. 2015; Prescott et al. 2015; Arrigoni Battaia et al. 2015a; Cai et al. 2017). The origins of LABs (LAEs with a diameter $\simeq 20 - 400$ kpc) are also explained by several mechanisms: (1) resonant scattering of Ly α photons emitted from central sources in dense and extended neutral hydrogen clouds (e.g., Hayes et al. 2011), (2) cooling radiation from gravitationally heated gas in collapsed halos (e.g., Haiman et al. 2000), (3) shock heating by galactic superwind originated from starbursts and/or AGN activity (e.g., Taniguchi & Shioya 2000), (4) galaxy major mergers (e.g., Yajima et al. 2013), and (5) photoionization by external UV sources (QSO fluorescence; e.g., Cantalupo et al. 2005). Moreover, LABs have been often discovered in over-density regions at $z \simeq 2 - 3$ (e.g., Yang et al. 2009; Yang et al. 2010; Matsuda et al. 2011). Thus, such LABs could be closely related to the galaxy environments, and might be linked to the formation mechanisms of central massive galaxies in galaxy protoclusters.

During the last decades, Suprime-Cam (SCam) on the Subaru telescope has led the world on identifying such rare Ly α -emitting populations at $z \gtrsim 6$ (LEW LAEs; e.g., Nagao et al. 2008; Kashikawa et al. 2012; LABs; e.g., Ouchi et al. 2009; Sobral et al. 2015). However, the formation mechanisms of these rare Ly α -emitting populations are still controversial due to the small statistics. While LEW LAEs and LABs at $z \simeq 2 - 5$ have been studied intensively with a sample of $\gtrsim 100$ sources, only a few sources have been found so far at $z \gtrsim 6$. Large-area NB data are required to carry out a statistical study on LEW LAEs and LABs at $z \gtrsim 6$.

In March 2014, the Subaru telescope has started a large-area NB survey using a new wide field of view (FoV) camera, Hyper Suprime-Cam (HSC) in a Subaru strategic program (SSP; Aihara et al. 2017b). In the five-year project, HSC equipped with four NB filters of *NB387*, *NB816*, *NB921*, and *NB101* will survey for LAEs at $z \simeq 2.2$, 5.7, 6.6, and 7.3, respectively. The HSC SSP NB survey data consist of two layers; Ultradeep (UD), and Deep (D), covering 2 fields (UD-COSMOS, UD-SXDS), and 4 fields (D-COSMOS, D-SXDS, D-DEEP2-3, D-ELAIS-N1), respectively. The *NB816*, *NB921*, and *NB101* images will be taken for the UD fields. The *NB387*, *NB816*, and *NB921* observations will be conducted in 15 HSC-pointing D fields.

Using the large HSC NB data complemented by optical and NIR spectroscopic observations, we launch a research project for Ly α -emitting objects: *Systematic Identification of LAEs for Visible Exploration and Reionization Research Using Subaru HSC (SILVERRUSH)*. The large LAE samples provided by SILVERRUSH enable us to investigate e.g., LAE clustering (Ouchi et al. 2017), LEW LAEs and LABs (this work), spec-

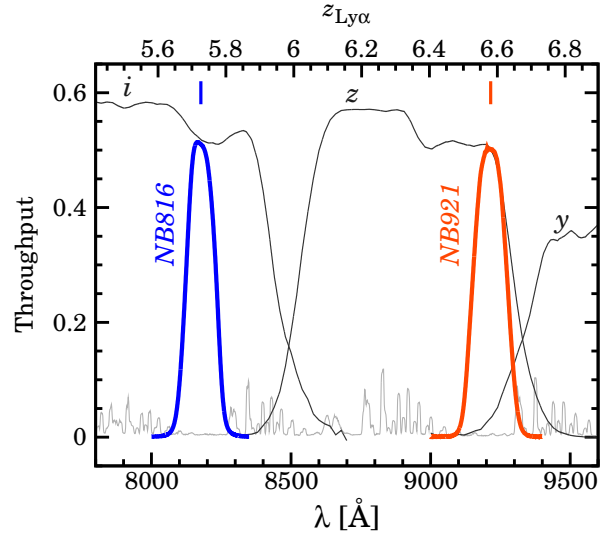


Fig. 1. Filter transmission curves of the NB and BB filters. The red and blue curves represent the *NB921* and *NB816* filters, respectively. The red and blue ticks show the NB central wavelengths with the same color coding as for the NB filter transmission curves. The black solid curves indicate the *i*, *z*, and *y*-band filters, from left to right. The gray line denotes the OH sky lines. The bandpass of these NB and BB filters corresponds to the area-weighted mean transmission curves¹. The transmission curves are derived by taking into account 1) the quantum efficiency of CCD, the transmittance of 2) the dewar window and 3) the HSC primary focus unit (POpt2), 4) the reflectivity of the primary mirror, and 5) the sky transparency (see Aihara et al. 2017a). The upper *x*-axis corresponds to the redshift of Ly α .

troscopic properties of bright LAEs (Shibuya et al. 2017b), Ly α luminosity functions (Konno et al. 2017), and LAE over-density (R. Higuchi et al. in preparation). The LAE survey strategy is given by Ouchi et al. (2017). This program is one of the twin programs. Another program is the study for dropouts, Great Optically Luminous Dropout Research Using Subaru HSC (GOLDRUSH), that is detailed in Ono et al. (2017), Harikane et al. (2017), and Toshikawa et al. (2017).

This is the second paper in the SILVERRUSH project. In this paper, we present LAE selection processes and machine-readable catalogs of the LAE candidates at $z \simeq 5.7 - 6.6$. Using the large LAE sample obtained with the first HSC NB data, we examine the redshift evolutions of Ly α EW distributions and LAB number density. This paper has the following structure. In Section 2, we describe the details of the SSP HSC data. Section 3 presents the LAE selection processes. In Section 4, we check the reliability of our LAE selection. Section 5 presents Ly α EW distributions and LABs at $z \simeq 6 - 7$. In Section 6, we discuss the physical origins of LEW LAEs and LABs. We summarize our findings in Section 7.

Throughout this page, we adopt the concordance cosmology with $(\Omega_m, \Omega_\Lambda, h) = (0.3, 0.7, 0.7)$ (Planck Collaboration et al. 2016). All magnitudes are given in the AB system (Oke & Gunn 1983).

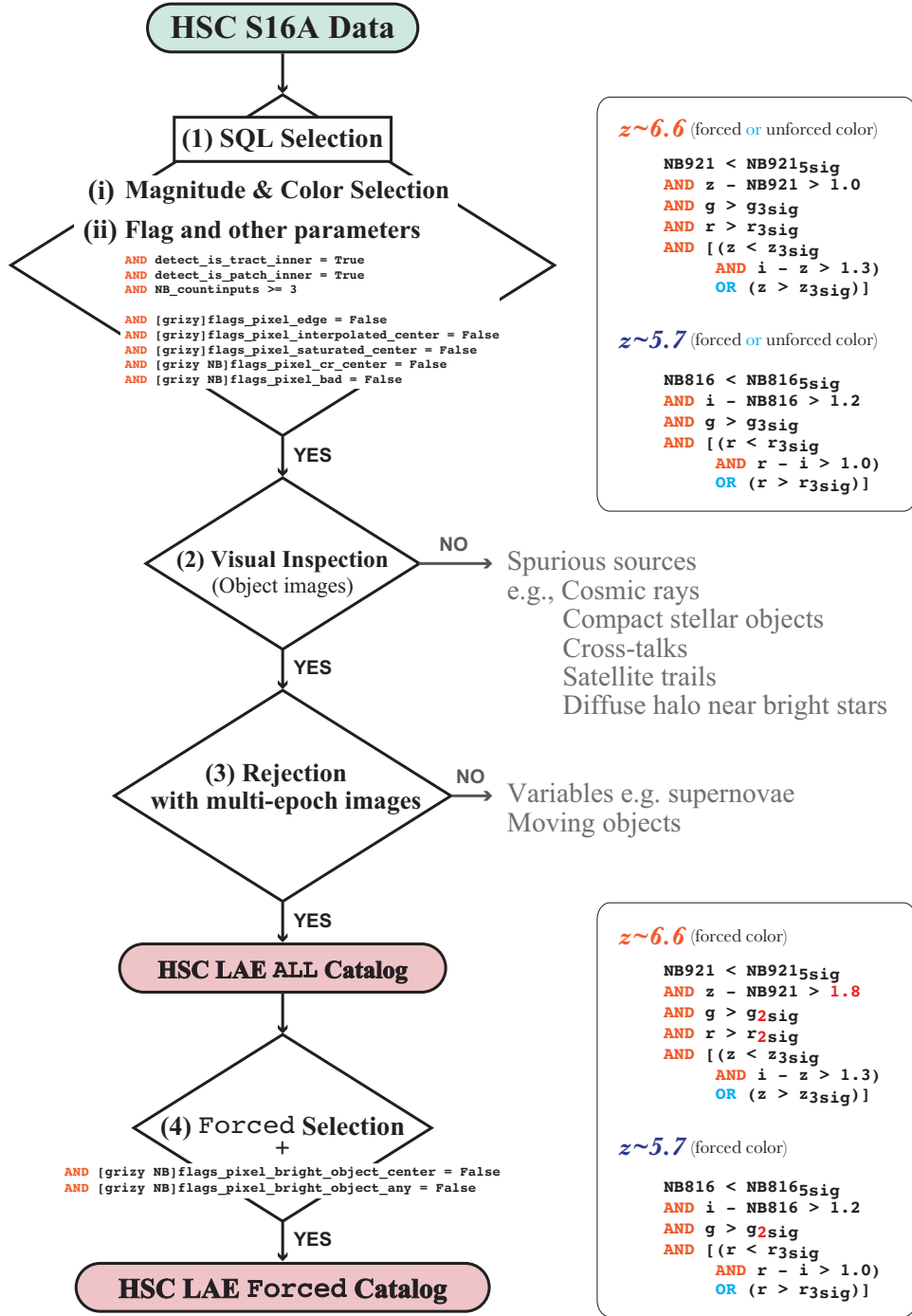


Fig. 2. Flow chart of the HSC LAE selection process. See Section 3 for more details.

2 HSC SSP Imaging Data

We use the HSC SSP S16A data products of g, r, i, z , and y broadband (BB; Kawanomoto 2017), $NB921$ and $NB816$ (Ouchi et al. 2017) images that are obtained in 2014–2016. It should be noted that this HSC SSP S16A data is significantly larger than the one of the first-data release in Aihara et al. (2017a). The $NB921$ ($NB816$) filter has a central wavelength

of $\lambda_c = 9215\text{\AA}$ (8177\AA) and an FWHM of $\Delta\lambda = 135\text{\AA}$ (113\AA), all of which are the area-weighted mean values. The $NB921$ and $NB816$ filters trace the redshifted Ly α emission lines at $z = 6.580 \pm 0.056$ and $z = 5.726 \pm 0.046$, respectively. The NB filter transmission curves are shown in Figure 1. The central wavelength, FWHM, and the bandpass shape for these NB filters are almost uniform over the HSC FoV. The deviation of the λ_c and FWHM values are typically within $\simeq 0.3\%$ and $\simeq 10\%$,

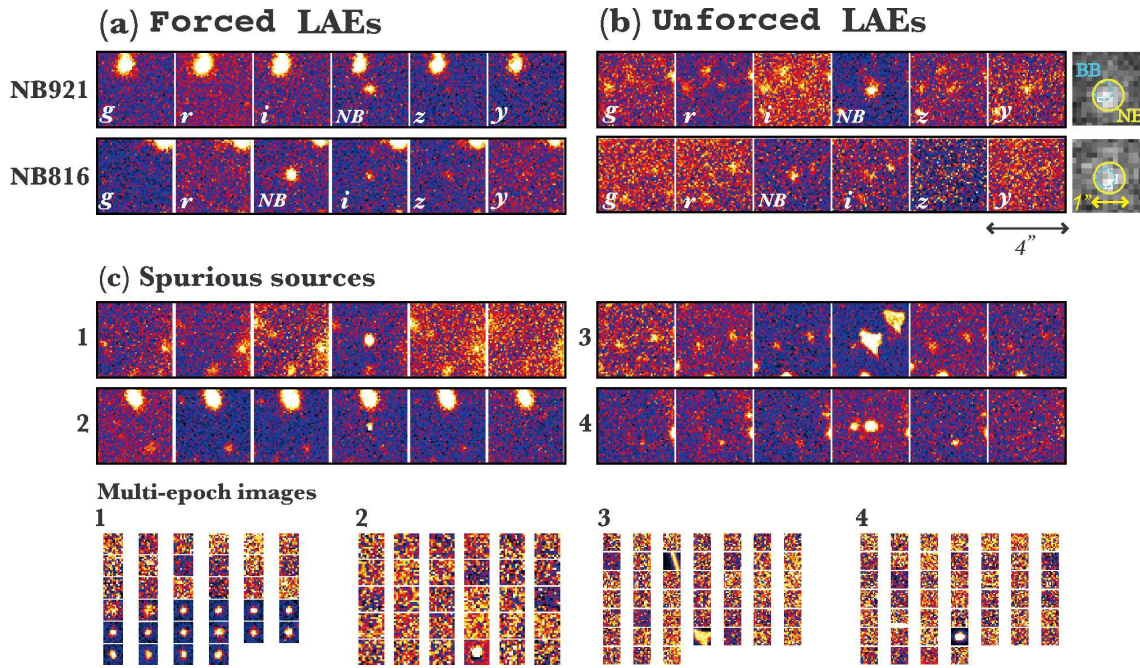


Fig. 3. Multi-band cutout images of our example LAEs and spurious sources. (a) LAEs at $z \simeq 6.6$ (top) and $z \simeq 5.7$ (bottom) in the forced LAE catalog. (b) LAEs at $z \simeq 6.6$ (top) and $z \simeq 5.7$ (bottom) in the unforced catalog. In the rightmost cutout images, the yellow solid and cyan dashed circles represent the central positions of the unforced LAEs in the NB and BB images, respectively. The diameters of the yellow solid and dashed circles in the cutout images of the unforced LAEs are $1''$ and $0.7''$, respectively. (c) Spurious sources with an NB magnitude-excess similar to that of LAE candidates (four panel sets at the top), 1: variable (e.g., supernova); 2: cosmic ray; 3: cross-talk artifact; 4: moving object (e.g., asteroids) and corresponding multi-epoch images (four panel sets at the bottom). The image size is $4'' \times 4''$ for the LAEs and spurious sources.

respectively. Thus, we use the area-weighted mean transmission curves in this study. The detailed specifications of these NB filters are given in Ouchi et al. (2017).

Table 1 summarizes the survey areas, exposure time, and depth of the HSC SSP S16A NB data. The current HSC SSP S16A NB data covers UD-COSMOS, UD-SXDS, D-COSMOS, D-DEEP2-3, D-ELAIS-N1 for $z \simeq 6.6$, and UD-COSMOS, UD-SXDS, D-DEEP2-3, D-ELAIS-N1 for $z \simeq 5.7$. The effective survey areas of the NB921 and NB816 images are 21.2 and 13.8 arcmin², corresponding to the survey volumes of $\simeq 1.9 \times 10^7$ and $\simeq 1.2 \times 10^7$ Mpc³, respectively. The area of these HSC NB fields are covered by the observations of all the BB filters. The typical limiting magnitudes of BB filters are $g \simeq 26.9$, $r \simeq 26.5$, $i \simeq 26.3$, $z \simeq 25.7$, and $y \simeq 25.0$ ($g \simeq 26.6$, $r \simeq 26.1$, $i \simeq 25.9$, $z \simeq 25.2$, and $y \simeq 24.4$) in a $1''.5$ aperture at 5σ for the UD (D) fields. The FWHM size of point spread function in the HSC images is typically $\simeq 0''.8$ (Aihara et al. 2017a).

The HSC images were reduced with the HSC pipeline, hscPipe 4.0.2 (Bosch et al. 2017) which is a code from the Large Synoptic Survey Telescope (LSST) software pipeline (Ivezic et al. 2008; Axelrod et al. 2010; Jurić et al. 2015). The HSC pipeline performs CCD-by-CCD reduction, calibration for astrometry, and photometric zero point determination. The pipeline then conducts mosaic-stacking that com-

bines reduced CCD images into a large coadd image, and create source catalogs by detecting and measuring sources on the coadd images. The photometric calibration is carried out with the PanSTARRS1 processing version 2 imaging survey data (Magnier et al. 2013; Schlafly et al. 2012; Tonry et al. 2012). The details of the HSC SSP survey, data reduction, and source detection and photometric catalog construction are provided in Aihara et al. (2017a), Aihara et al. (2017b), and Bosch et al. (2017).

In the HSC images, source detection and photometry were carried out in two methods: unforced and forced. The unforced photometry is a method to perform measurements of coordinates, shapes, and fluxes individually in each band image for an object. The forced photometry is a method to carry out photometry by fixing centroid and shape determined in a reference band and applying them to all the other bands. The algorithm of the forced detection and photometry is similar to the double-image mode of SExtractor (Bertin & Arnouts 1996) that are used in most of the previous studies for high- z galaxies. According to which depends on magnitudes, S/N , positions, and profiles for detected sources, one of the BB and NB filter is regarded as a reference band. For merging the catalogs of each band, the object matching radius is not a specific value which depends on an area of regions with a $> 5\sigma$ sky noise level. We refer the detailed algorithm to choose the reference filter and

filter priority to Bosch et al. (2017).

In the *hscPipe* detection and photometry, an NB filter is basically chosen as a reference band for the NB-bright and BB-faint sources such as LAEs. However, a BB filter is used as a reference band in the case that sources are bright in the BB image. The current version of *hscPipe* has not implemented the NB-reference forced photometry for BB-bright sources. In this specification, there is a possibility that we miss BB-bright sources with a spatial offset between centroids of BB and NB by using only the forced photometry. Thus, we combine the unforced or forced photometry for *BB - NB* colors to identify such BB-bright objects with a spatial offset between centroids of BB and NB (e.g., Shibuya et al. 2014a). See Section 3 for details of the LAE selection criteria.

We use *cmodel* magnitudes for estimating total magnitudes of sources. The *cmodel* magnitude is a weighted combination of exponential and de Vaucouleurs fits to light profiles of each object. The detailed algorithm of the *cmodel* photometry are presented in Bosch et al. (2017). To measure the *S/N* values for source detections, we use $1.''5$ -diameter aperture magnitudes.

3 LAE Selection

Using the HSC data, we perform a selection for LAEs at $z \simeq 6.6$ and $\simeq 5.7$. Basically, we select objects showing a significant flux excess in the NB images and a spectral break at the wavelength of redshifted $\text{Ly}\alpha$ emission. In this study, we create two LAE catalogs: *HSC LAE ALL (forced+unforced) catalog* and *HSC LAE forced catalog*. The HSC LAE ALL catalog is constructed in a combination of the forced and unforced photometry. We use this HSC LAE ALL catalog for identifying objects with a spatial offset between centroids of BB and NB (see Section 2). On the other hand, the HSC LAE forced catalog consists of LAEs meeting only the selection criteria of the forced photometry. We use this HSC LAE forced catalog for statistical studies for LAEs (e.g., $\text{Ly}\alpha$ LFs). The HSC LAE forced catalog is a subsample of the ALL one. Figure 2 shows the flow chart of the LAE selection process. We carry out the following processes: (1) SQL selection, (2) visual inspections for the object images, (3) rejections of variable and moving objects with the multi-epoch images, and (4) forced selection. The details are described as below.

- (1) **SQL selection:** We retrieve detection and photometric catalogs from PostgreSQL database tables. Using SQL scripts, we select objects meeting the following criteria of (i) magnitude and color selections and (ii) *hscPipe* parameters and flags.
 - (i) **Magnitude and color selection:** To identify objects with an *NB* magnitude excess in the HSC catalog, we apply the magnitude and color selection criteria that are similar to e.g., Ouchi et al. 2008; Ouchi et al. 2010:

$$\begin{aligned}
 & \text{NB921}_{\text{frc}}^{\text{ap}} < \text{NB921}_{5\sigma} \\
 & \&\& (g_{\text{frc}} > g_{3\sigma} \parallel g_{\text{frc}}^{\text{ap}} > g_{3\sigma}) \\
 & \&\& (r_{\text{frc}} > r_{3\sigma} \parallel r_{\text{frc}}^{\text{ap}} > r_{3\sigma}) \\
 & \&\& (z_{\text{frc}} - \text{NB921}_{\text{frc}} > 1.0 \parallel z_{\text{unf}} - \text{NB921}_{\text{unf}} > 1.0) \quad (1) \\
 & \&\& \{ [(z_{\text{frc}} < z_{3\sigma} \parallel z_{\text{frc}}^{\text{ap}} < z_{3\sigma}) \\
 & \quad \&\& (i_{\text{frc}} - z_{\text{frc}} > 1.3 \parallel i_{\text{unf}} - z_{\text{unf}} > 1.3)] \\
 & \quad \parallel (z_{\text{frc}} > z_{3\sigma} \parallel z_{\text{frc}}^{\text{ap}} > z_{3\sigma}) \} ,
 \end{aligned}$$

for $z \simeq 6.6$, and,

$$\begin{aligned}
 & \text{NB816}_{\text{frc}}^{\text{ap}} < \text{NB816}_{5\sigma} \\
 & \&\& (g_{\text{frc}} > g_{3\sigma} \parallel g_{\text{frc}}^{\text{ap}} > g_{3\sigma}) \\
 & \&\& (i_{\text{frc}} - \text{NB816}_{\text{frc}} > 1.2 \parallel i_{\text{unf}} - \text{NB816}_{\text{unf}} > 1.2) \quad (2) \\
 & \&\& \{ [(r_{\text{frc}} < r_{3\sigma} \parallel r_{\text{frc}}^{\text{ap}} < r_{3\sigma}) \\
 & \quad \&\& (r_{\text{frc}} - i_{\text{frc}} > 1.0 \parallel r_{\text{unf}} - i_{\text{unf}} > 1.0)] \\
 & \quad \parallel (r_{\text{frc}} > r_{3\sigma} \parallel r_{\text{frc}}^{\text{ap}} > r_{3\sigma}) \} ,
 \end{aligned}$$

for $z \simeq 5.7$, where the indices of *frc* and *unf* represent the forced and unforced photometry, respectively. The subscript of 5σ (3σ) indicates the 5σ (3σ) limiting magnitude for a given filter. The values with and without a superscript of *ap* indicate the aperture and total magnitudes, respectively. These magnitudes are derived with the *hscPipe* software (see Section 2; Bosch et al. 2017). The limits of the *i - NB816* and *z - NB921* colors are the same as those of Ouchi et al. (2008) and Ouchi et al. (2010), respectively. To exploit the survey capability of HSC identifying rare objects, we use the 3σ *g* and *r* limiting magnitude (instead of the value of 2σ used in Ouchi et al. 2008) for the criteria of Lyman break off-band non-detection. In the process (4), we replace 3σ with 2σ for the *g* and *r* magnitude criteria for the consistency with the previous studies.

Note that we do not apply the `flags.pixel.bright_object.[center/any]` masking to the LAE ALL catalog in order to maximize LAE targets for future follow-up observations (Aihara et al. 2017a). These flags for the object masking are used in the process (4).

- (ii) **Parameters and flags:** Similar to Ono et al. (2017), we set several *hscPipe* parameters and flags in the HSC catalog to exclude e.g., blended sources, and objects affected by saturated pixels, and nearby bright source halos. We also mask regions where exposure times are relatively short by using the `countinputs` parameter, N_c , which denotes the number of exposures at a source position for a given filter. Table 2 summarizes the values and brief explanations of the *hscPipe* parameters and flags used for our LAE selection. The full details of these parameters and flags are presented in Aihara et al. (2017a). To search for LAEs in large areas of the HSC fields, we do not apply the `countinputs` parameter to the BB images.

Table 1. Properties of the HSC SSP S16A NB Data

Field	R.A. (J2000)	Dec. (J2000)	Area (deg ²)	T_{exp} (hour)	$m_{\text{lim}}(5\sigma, 1.5''\phi)$ (mag)	$N_{\text{LAE,ALL}}$	$N_{\text{LAE,F}}$
(1)	(2)	(3)	(4)	(5)	(6)	(7)	(8)
<i>NB921</i> ($z \simeq 6.6$)							
UD-COSMOS	10:00:28	+02:12:21	2.05	11.25	25.6	338	116
UD-SXDS	02:18:00	−05:00:00	2.02	7.25	25.5	58	23
D-COSMOS	10:00:60	+02:13:53	5.31	2.75	25.3	244 ^a	47 ^a
D-DEEP2-3	23:30:22	−00:44:38	5.76	1.00	24.9	164	35
D-ELAIS-N1	16:10:00	+54:17:51	6.08	1.75	25.3	349	48
Total	—	—	21.2	24.00	—	1153	269
<i>NB816</i> ($z \simeq 5.7$)							
UD-COSMOS	10:00:28	+02:12:21	1.97	5.50	25.7	201	176
UD-SXDS	02:18:00	−05:00:00	1.93	3.75	25.5	224	188
D-DEEP2-3	23:30:22	−00:44:38	4.37	1.00	25.2	423	282
D-ELAIS-N1	16:10:00	+54:17:51	5.56	1.00	25.3	229	130
Total	—	—	13.8	11.25	—	1077	776

(1) Field.

(2) Right ascension.

(3) Declination.

(4) Survey area with the HSC SQL parameters in Table 2.

(5) Total exposure time of the NB imaging observation.

(6) Limiting magnitude of the NB image defined by a 5σ sky noise in a $1.5''$ diameter circular aperture.

(7) Number of the LAE candidates in the ALL (unforced+forced) catalog.

(8) Number of the LAE candidates in the forced catalog.

^a The value of $N_{\text{LAE,ALL}}$ ($N_{\text{LAE,F}}$) includes 30 (7) LAEs selected in UD-COSMOS.**Table 2.** HSC SQL Parameters and Flags for Our LAE Selection

Parameter or Flag	Value	Band	Comment
detect_is_tract_inner	True	—	Object is in an inner region of a tract and not in the overlapping region with adjacent tracts
detect_is_patch_inner	True	—	Object is in an inner region of a patch and not in the overlapping region with adjacent patches
countinputs	≥ 3	<i>NB</i>	Number of visits at a source position for a given filter.
flags_pixel_edge	False	<i>grizy, NB</i>	Locate within images
flags_pixel_interpolated_center	False	<i>grizy, NB</i>	None of the central 3×3 pixels of an object is interpolated
flags_pixel_saturated_center	False	<i>grizy, NB</i>	None of the central 3×3 pixels of an object is saturated
flags_pixel_cr_center	False	<i>grizy, NB</i>	None of the central 3×3 pixels of an object is masked as cosmic ray
flags_pixel_bad	False	<i>grizy, NB</i>	None of the pixels in the footprint of an object is labelled as bad

The number of objects selected in this process is $n_{\text{SQL}} \simeq 121,000$.

- (2) **Visual inspections for object images:** To exclude cosmic rays, cross-talks, compact stellar objects, and artificial diffuse objects, we perform visual inspections for the BB and NB images of all the objects selected in the process (1). Most spurious sources are diffuse components near bright stars and extended nearby galaxies. The hscPipe software conducts the cmodel fit to broad light profiles of such diffuse sources in the NB images, which enhances the *BB* – *NB*

colors. For this reason, the samples constructed in the current SQL selection are contaminated by many diffuse components. Due to the clear difference of the appearance between LAE candidates and diffuse components, such spurious sources can be easily excluded through the visual inspections. The number of objects selected in this process is $n_{\text{vis}} \simeq 10,900$.

The visual inspection processes are mainly conducted by one of the authors. For the reliability check, four authors in this paper have individually carried out such visual inspections

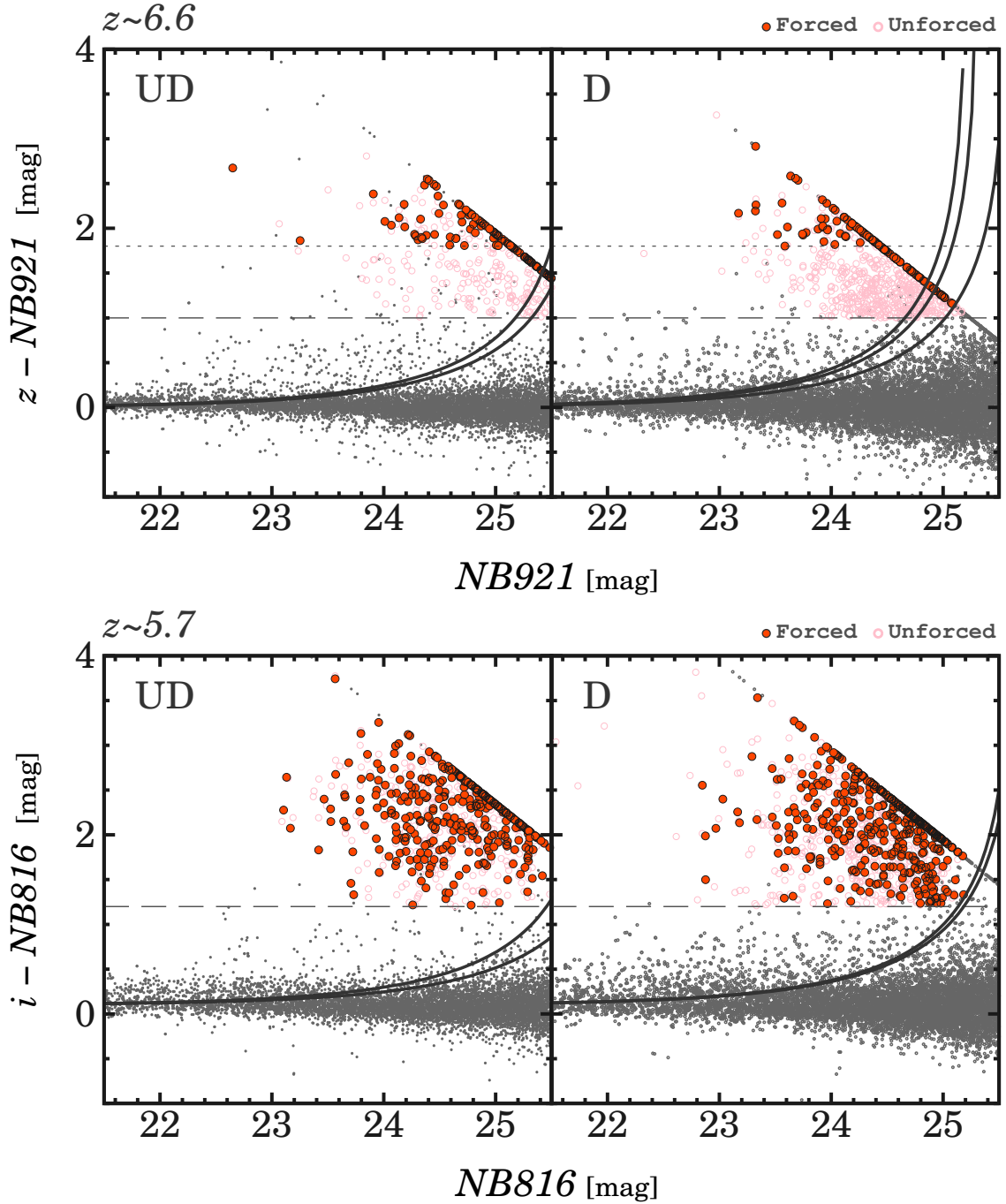


Fig. 4. (Top) Color of $z - \text{NB921}$ as a function of NB921 magnitude for the LAEs at $z \simeq 6.6$ in the UD (left) and D (right) fields. The filled red and open magenta circles denote the forced and unforced LAEs, respectively. For the LAEs undetected in the z -band images, the z -band magnitudes are replaced with the 2σ limiting magnitudes. The x-axis denotes the forced (unforced) $z - \text{NB921}$ colors for the forced (unforced) LAEs. The horizontal dashed and dotted line shows the color criteria of $z - \text{NB921} > 1.0$ and $z - \text{NB921} > 1.8$, respectively. The gray dots present objects detected in the NB921 images. The solid curves show the 3σ error tracks of $z - \text{NB921}$ color for each field. The 3σ error tracks are derived by Equation 3. (Bottom) Color of $i - \text{NB816}$ as a function of NB816 magnitude for the LAEs at $z \simeq 5.7$. The definitions of symbols, curves, and lines are the same as those of the top panels.

for $\simeq 5,300$ objects in the UD-COSMOS NB816 fields, and compare the results of the LAE selection. The difference in the number of selected LAEs is within ± 5 objects. Thus, we do not find a large difference in our visual inspection results.

(3) Rejection of variable and moving objects with multi-

epoch images: We exclude variable and moving objects such as supernovae, AGNs, satellite trails, and asteroids using multi-epoch NB images. The NB images were typically taken a few months - years after the BB imaging observations. For this reason, there is a possibility that sources with

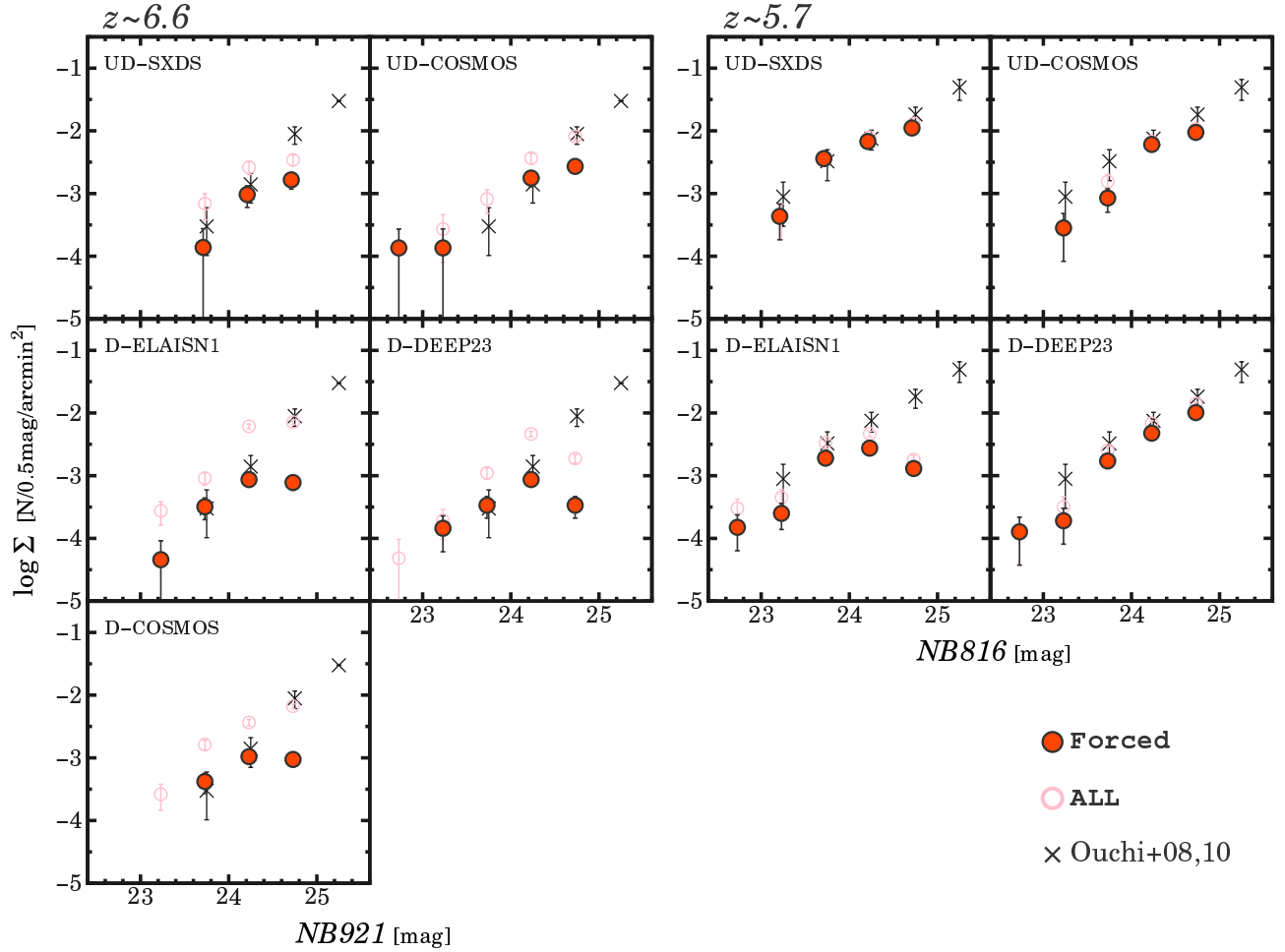


Fig. 5. Surface number density (SND) of the HSC LAEs at $z \simeq 6.6$ (five panels at the left) and $\simeq 5.7$ (four panels at the right) in each UD and D field. The filled red and open magenta circles indicate the LAEs in the forced and ALL catalog, respectively. The error bars are given by Poisson statistics from the number of LAEs. The gray crosses represent the LAEs in Ouchi et al. (2010) for $z \simeq 6.6$ and Ouchi et al. (2008) for $z \simeq 5.7$. The data points of the gray crosses are identical in all the fields for each redshift. The SND slight declines in the HSC LAEs at $NB \gtrsim 24.5$ mag would be originated from the incompleteness of the LAE detection and selection. The completeness-corrected SNDs are presented in Konno et al. (2017). The data points of the HSC LAEs are slightly shifted along x-axis for clarity.

an NB flux excess are variable or moving objects which happened to enhance the luminosities during the NB imaging observations.

The NB images are created by coadding $\simeq 10 - 20$ and $\simeq 3 - 5$ frames of 15 minute exposures for the current HSC UD and D data, respectively. Using the multi-epoch images, we automatically remove the variable and moving objects as follows. First, we measure the flux for individual epoch images, $f_{1\text{epoch}}$, for each object. Next, we obtain an average, f_{ave} , and a standard deviation, σ_{epoch} , from a set of the $f_{1\text{epoch}}$ values after a 2σ flux clipping. Finally, we discard an object having at least a multi-epoch image with a significantly large $f_{1\text{epoch}}$ value of $f_{1\text{epoch}} \geq f_{\text{ave}} + A_{\text{epoch}} \times \sigma_{\text{epoch}}$. Here we tune the A_{epoch} factor based on the depth of the NB fields. The A_{epoch} value is typically $\simeq 2.0 - 2.5$. Figure 3 shows examples of the spurious sources.

We also perform visual inspections for multi-epoch images

to remove contaminants which are not excluded in the automatic rejection above. We refer the remaining objects after this process as the LAE ALL catalog.

(4) Forced selection:

In the selection criteria of Equations (1) and (2), the HSC LAE ALL catalog is obtained in the combination of the forced and unforced colors. In this process, we select LAEs only with the forced color excess to create the forced LAE subsamples from the HSC LAE ALL catalog. In addition, the 3σ limit is replaced with 2σ for the criteria of g and r band non-detections.

Here we also adopt a new stringent color criterion of $z - NB921 > 1.8$ for $z \simeq 6.6$ LAEs. Due to the difference of the z band transmission curves between SCam and HSC, the criterion of $z - NB921 > 1.0$ in Equation (1) do not allow us to select LAEs whose $EW_{0,\text{Ly}\alpha}$ is similar to those of previous SCam studies. The $BB - NB$ color crite-

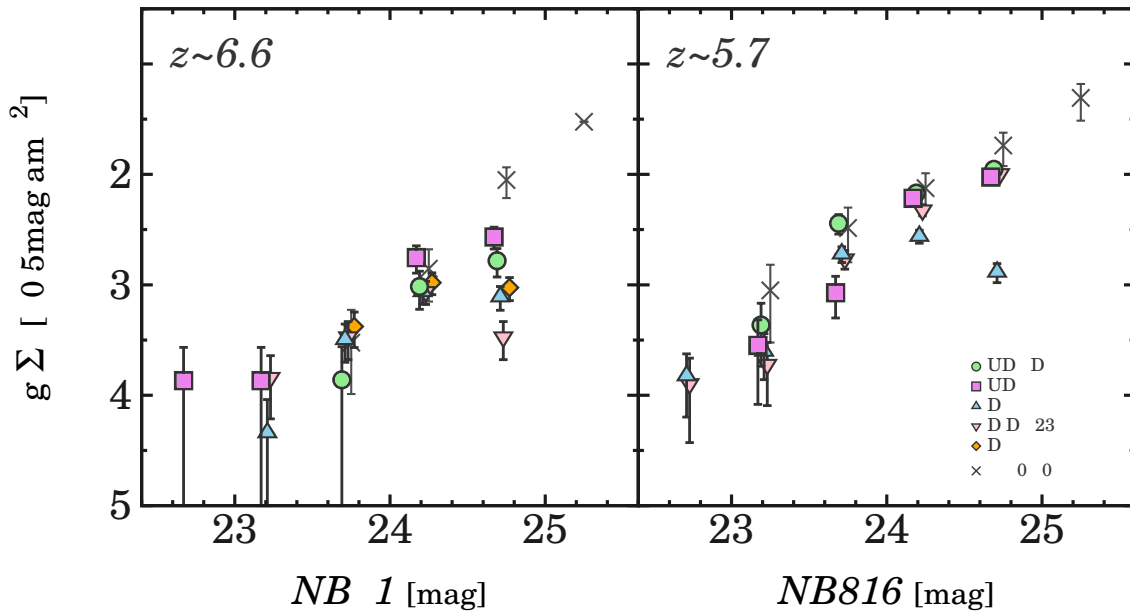


Fig. 6. Surface number density (SND) as a function of NB magnitude for the LAEs at $z \sim 6.6$ (left) and ~ 5.7 (right) in the HSC LAE forced catalog. The colored symbols denote the LAEs in each UD and D field (green circles: UD-SXDS; magenta squares: UD-COSMOS; cyan triangles: D-ELAIS-N1; light-red inverse-triangles: D-DEEP2-3; orange diamonds: D-COSMOS). The error bars are given by Poisson statistics from the number of LAEs. The gray crosses represent the LAEs in Ouchi et al. (2010) for $z \sim 6.6$ and Ouchi et al. (2008) for $z \sim 5.7$. The SND slight declines in the HSC LAEs at $NB \gtrsim 24.5$ mag would be originated from the incompleteness of the LAE selection. The completeness-corrected SNDs are presented in Konno et al. (2017). The data points of the HSC LAEs are slightly shifted along x-axis for clarity.

Table 3. Photometric properties of example LAE candidates

Object ID	NB	g	r	i	z	y
(1)	(mag)	(mag)	(mag)	(mag)	(mag)	(mag)
(1)	(2)	(3)	(4)	(5)	(6)	(7)
UD-SXDS ($NB921$)						
HSC J021601–041442	23.85 ± 0.10	26.89 ± 0.45	27.03 ± 0.62	26.65 ± 0.63	25.28 ± 0.31	25.29 ± 0.53
HSC J021754–051454	24.01 ± 0.12	> 27.6	> 27.3	> 26.9	26.09 ± 0.57	25.21 ± 0.50
HSC J021702–050604	24.64 ± 0.21	> 27.6	> 27.3	> 26.9	> 26.5	> 25.8
HSC J021638–043228	24.74 ± 0.23	> 27.6	> 27.3	> 26.9	26.17 ± 0.60	> 25.8
HSC J021609–050236	24.90 ± 0.26	27.53 ± 0.72	27.29 ± 0.75	> 26.9	26.32 ± 0.67	> 25.8
UD-COSMOS ($NB816$)						
HSC J100243+024551	23.69 ± 0.08	> 27.6	> 27.3	26.49 ± 0.53	> 26.6	> 25.8
HSC J100239+022806	24.14 ± 0.13	> 27.6	> 27.3	26.76 ± 0.64	26.12 ± 0.54	> 25.8
HSC J100243+015931	24.63 ± 0.19	> 27.6	> 27.3	> 27.0	> 26.6	> 25.8
HSC J095936+014108	25.02 ± 0.26	> 27.6	> 27.3	> 27.0	> 26.6	> 25.8
HSC J100245+021536	25.15 ± 0.29	> 27.6	> 27.3	> 27.0	> 26.6	> 25.8

(1) Object ID.

(2)-(7) Total magnitude of NB -, g -, r -, i -, z -, and y -bands.

The 2σ limits of the total magnitudes for the undetected bands.

(The complete machine-readable catalogs will be available on our project webpage at <http://cos.icrr.u-tokyo.ac.jp/rush.html>.)

ria in the forced selection correspond to the rest-frame $\text{Ly}\alpha$ EW of $EW_{0,\text{Ly}\alpha} > 14 \text{ \AA}$ and $> 10 \text{ \AA}$ for $z \sim 6.6$ and $z \sim 5.7$ LAEs, respectively. These $EW_{0,\text{Ly}\alpha}$ limits are comparable to those of the previous SCam studies (e.g., Ouchi et al. 2010). The relation between $EW_{0,\text{Ly}\alpha}$ and $BB -$

NB colors is described in Konno et al. (2017) in details. Moreover, we remove the objects in masked regions defined by the `flags_pixel_bright_object_[center/any]` parameters (Aihara et al. 2017a).

We refer the set of the remaining objects after this process as

the forced LAE catalog. This forced LAE catalog is used for studies on LAE statistics such as measurements of Ly α EW scale lengths.

The LAE candidates selected in this forced selection are referred to as the forced LAEs. On the other hand, we refer to the remaining LAE candidates in the HSC LAE ALL catalog as the unforced LAEs. The examples of forced and unforced LAEs are shown in Figure 3. As shown in the top-right panels of Figure 3, the unforced LAEs have a $\simeq 0''.2 - 0''.3$ spatial offset between centroids in NB and BB.

In total, we identify 2,230 and 1,045 LAE candidates in the HSC LAE ALL and forced catalogs, respectively. Table 1 presents the numbers of LAE candidates in each field. The machine-readable catalogs of all the LAE candidates will be provided on our project webpage at <http://cos.icrr.u-tokyo.ac.jp/rush.html>. The photometric properties of example LAE candidates are shown in Table 3.

As shown in Table 1, the number of $z \simeq 5.7$ LAEs in D-DEEP2-3 appears to be large compared to that of the other $z \simeq 5.7$ fields. This may be because the seeing of the NB816 images of D-DEEP2-3 is better than that of the other $z \simeq 5.7$ fields. Similarly, the small number of $z \simeq 6.6$ LAEs in UD-SXDS may be affected by the seeing size. The number density of LAEs is discussed in the next section. Note that edge regions of UD-COSMOS is overlapped with a flanking field, D-COSMOS (Aihara et al. 2017b). We find that 30 (7) LAEs in UD-COSMOS are also selected in the HSC LAE ALL (forced) sample of D-COSMOS. To analyze the D field independently in the following sections, we include the overlapped LAEs in the D-COSMOS sample.

Figure 4 shows the color-magnitude diagrams for the LAE candidates. The solid curves in the color magnitude diagrams indicate the 3σ errors of $BB - NB$ color as a function of the NB flux, f_{NB} , given by

$$\pm 3\sigma_{BB-NB} = -2.5 \log_{10} \left(1 \mp 3 \frac{\sqrt{f_{1\sigma NB}^2 + f_{1\sigma BB}^2}}{f_{NB}} \right), \quad (3)$$

where $f_{1\sigma NB}$ and $f_{1\sigma BB}$ are the 1σ flux error in the z and NB921 (i and NB816) bands for $z \simeq 6.6$ ($z \simeq 5.7$), respectively. As shown in Figure 4, the LAE candidates have a significant NB magnitude excess.

4 Checking the Reliability of Our LAE Selection

Here we check the reliability of our LAE selection.

4.1 Spectroscopic Confirmations

We have conducted optical spectroscopic observations with Subaru/FOCAS and Magellan/LDSS3 for 18 bright LAE candidates with $NB \lesssim 24$ mag. In these observations, we have

confirmed 13 LAEs. By investigating our spectroscopic catalog of Magellan/IMACS, we also spectroscopically identify 8 LAEs with $NB \lesssim 24$ mag. In addition, we find that 75 LAEs are spectroscopically confirmed in literature (Murayama et al. 2007; Ouchi et al. 2008; Taniguchi et al. 2009; Ouchi et al. 2010; Mallery et al. 2012; Sobral et al. 2015; Higuchi et al. in preparation). In total, 96 LAEs have been confirmed in our spectroscopy and previous studies. Using the spectroscopic sample whose number of observed LAEs is known, we estimate the contamination rate to be $\simeq 0 - 30\%$. The details of the spectroscopic observations and contamination rates are given by Shibuya et al. (2017b).

4.2 LAE Surface Number Density

Figure 5 shows the surface number density (SND) of our LAE candidates and LAEs identified in previous Subaru/SCam NB surveys, SCam LAEs (e.g., Ouchi et al. 2008; Ouchi et al. 2010). We find that the SNDs of the forced LAEs are comparable to those of SCam LAEs. On the other hand, the SNDs of unforced LAEs at $z \simeq 6.6$ are higher than that of SCam LAEs. The high SND of the unforced LAEs is mainly caused by the color criterion for the HSC LAE ALL catalog of $z - NB921 > 1.0$ that is less stringent than $z - NB921 > 1.8$ (see Section 3). We also identify SND humps of our forced LAEs at $z \simeq 6.6$ at the bright-end of $NB \simeq 23$ mag in UD-COSMOS. The presence of such a SND hump has been reported by $z \simeq 6.6$ LAE studies (e.g., Matthee et al. 2015). The significance of the bright-end hump existence in Ly α LFs is $\simeq 3\sigma$, which are discussed in Konno et al. (2017). The slight declines in SNDs at a faint NB magnitude of $NB \gtrsim 24.5$ mag would be originated from the incompleteness of the LAE detection and selection. Konno et al. (2017) present the SND corrected for the incompleteness.

Figure 6 compiles the SNDs of all the HSC UD and D fields. We find that our SNDs show a small field-to-field variation, but typically follow those of the SCam LAEs.

4.3 Matching Rate of HSC LAEs and SCam LAEs

The UD-SXDS field has been observed previously by SCam equipped with the NB921 and NB816 filters (Ouchi et al. 2008; Ouchi et al. 2010). We compare the catalogs of our selected HSC LAE candidates and SCam LAEs, and calculate the object matching rates as a function of NB magnitudes. The object matching radius is $1''$. The object matching rate between the HSC LAEs and SCam LAEs is $\simeq 90\%$ at a bright NB magnitudes of $\lesssim 24$ mag. The high object matching rate indicates that we adequately identify LAEs in our selection processes. However, the matching rate decreases to $\simeq 70\%$ at a faint magnitude of $\simeq 24.5$ mag. This is due to the shallow depth of the HSC NB fields compared to the SCam ones. Konno et al. (2017) discuss the detection completeness of faint LAEs.

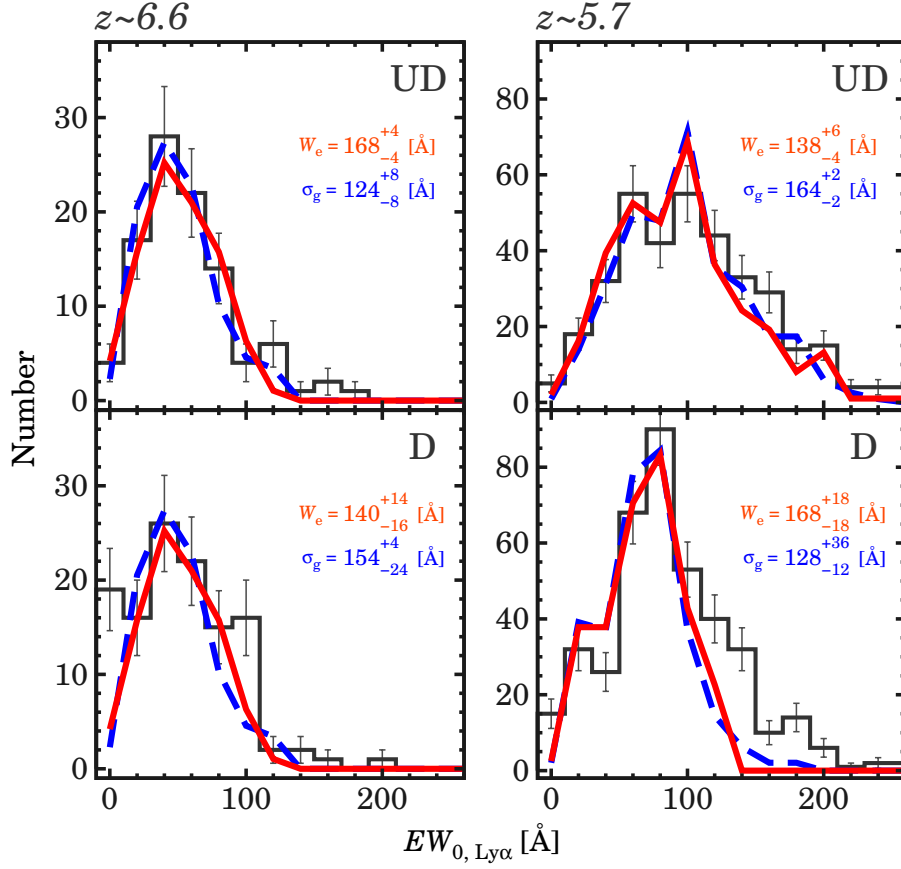


Fig. 7. Ly α EW distribution for the HSC LAEs at $z \simeq 6.6$ (left) and $z \simeq 5.7$ (right). The top and bottom panels show the UD and D fields, respectively. The thin gray histograms with error bars denote the Ly α EW distributions for the forced LAEs. The error bars are given by Poisson statistics from the number of sample LAEs. The red solid and blue dashed lines present the best-fit exponential and Gaussian functions of Equations (4) and (5), respectively, which are obtained from MC simulations with the $EW_{0, \text{Ly}\alpha}$ uncertainties (see Section 5.1 for more details).

5 Results

Here we present the Ly α EW distributions (Section 5.1) and LABs selected with the HSC data (Section 5.2). For the consistency with previous LAE studies, we use the forced LAE sample in the following analyses, if not specified.

5.1 Ly α EW Distribution

We present the Ly α EW distributions for LAEs at $z \simeq 5.7 - 6.6$. In a method described in Section 8, we calculate the rest-frame Ly α EW, $EW_{0, \text{Ly}\alpha}$, for the LAEs. The $y(z)$ band magnitudes are used for the rest-frame UV continuum emission of $z \simeq 6.6$ ($z \simeq 5.7$) LAEs. Figure 7 shows the observed Ly α EW distributions at $z \simeq 5.7 - 6.6$ in the UD and D fields. To quantify these Ly α EW distributions we perform Monte Carlo (MC) simulations. The procedure of the MC simulations is similar to that of e.g., Shimasaku et al. (2006), Ouchi et al. (2008) and Zheng et al. (2014). First, we generate artificial LAEs in a Ly α luminosity range of $\log L_{\text{Ly}\alpha} / \text{erg s}^{-1} = 42 - 44$ according to $z \simeq 5.7 - 6.6$ Ly α LFs of Konno et al. (2017). Next,

we assign Ly α EW and BB magnitudes to each LAE by assuming that the Ly α EW distributions are the exponential and Gaussian functions (e.g., Gronwall et al. 2007; Kashikawa et al. 2011; Oyarzún et al. 2016):

$$\frac{dN}{dEW} = N \exp\left(-\frac{EW}{W_e}\right), \quad (4)$$

and,

$$\frac{dN}{dEW} = N \frac{1}{\sqrt{2\pi\sigma_g^2}} \exp\left(-\frac{EW^2}{2\sigma_g^2}\right), \quad (5)$$

where N is the galaxy number, W_e and σ_g are the Ly α EW scale lengths of the exponential and Gaussian functions, respectively. By changing the intrinsic W_e and σ_g values, we make samples of artificial Ly α EW distributions. We then select LAEs based on NB and BB limiting magnitudes and $BB - NB$ colors corresponding to Ly α EW limits which are the same as those of our LAE selection criteria (Section 3). Finally, the best-fit Ly α EW scale lengths are obtained by fitting to the artificial Ly α EW distribution to the observed ones.

Figure 7 presents the Ly α EW distributions obtained in the MC simulations. As shown in Figure 7, we find that the Ly α

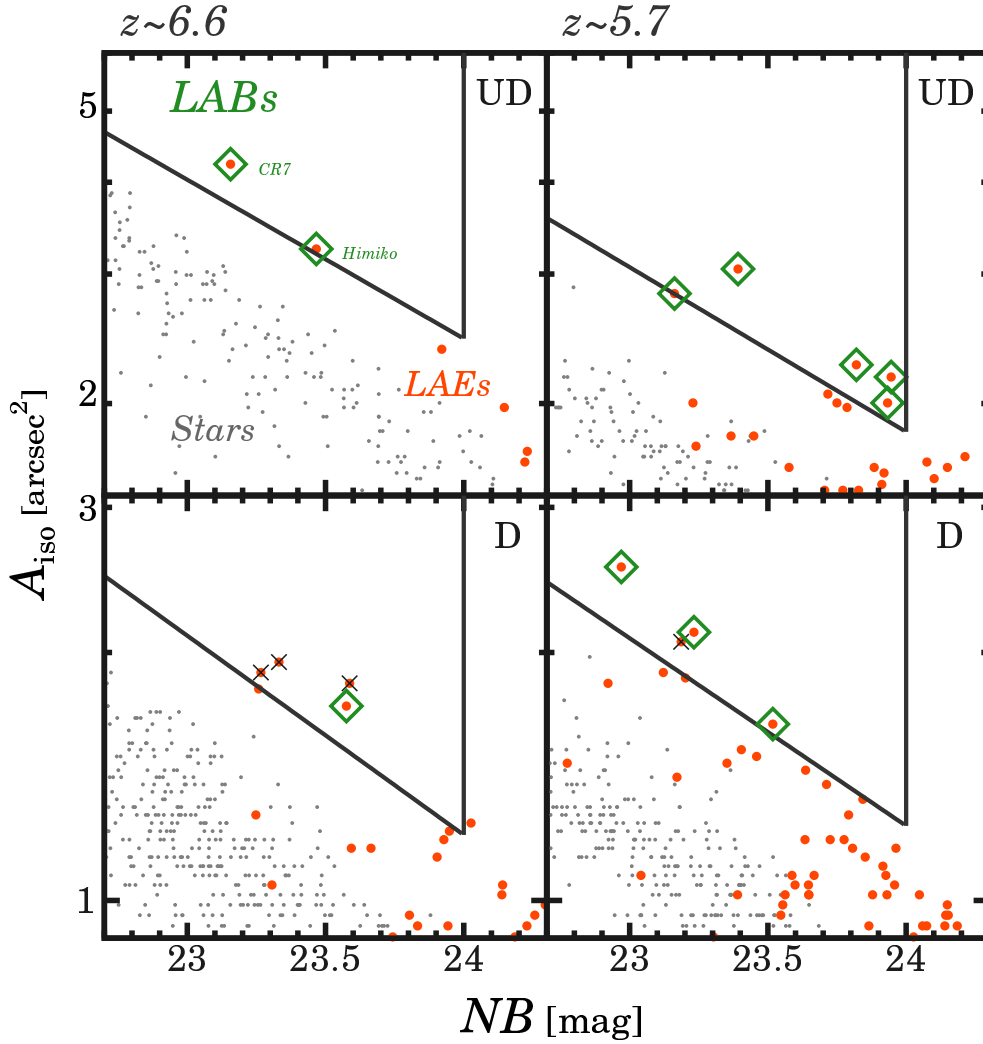


Fig. 8. Isophotal area, A_{iso} , as a function of NB magnitude to select LABs at $z \simeq 6.6$ (left) and $z \simeq 5.7$ (right). The top and bottom panels show the UD and D fields, respectively. The green diamonds denote the LABs. The filled red circles indicate the LAEs in the forced catalog. The gray dots represent star-like point sources selected in the HSC NB images. The diagonal and vertical lines denote the LAB selection criteria of A_{iso} and NB magnitude. The diagonal lines are defined by the 2.5σ deviation from the A_{iso} -NB magnitude distribution for the star-like point sources. The filled red circles with a cross indicate unreliable LAB candidates which are affected by e.g., diffuse halos of nearby bright stars. The $z \simeq 6.6$ LABs in the UD fields are CR7 (Sobral et al. 2015) and Himiko (Ouchi et al. 2009).

EW distributions are reasonably explained by the exponential and Gaussian profiles. The best-fit scale lengths are summarized in Table 5. The best-fit exponential (Gaussian) $\text{Ly}\alpha$ scale lengths are, on average of the UD and D fields, $153 \pm 18 \text{ \AA}$ and $154 \pm 15 \text{ \AA}$ ($146 \pm 24 \text{ \AA}$ and $139 \pm 14 \text{ \AA}$) at $z \simeq 5.7$ and $z \simeq 6.6$, respectively. As shown in Table 5, there is no large difference in the $\text{Ly}\alpha$ EW scale lengths for the UD and D fields. This no large $EW_{0,\text{Ly}\alpha}$ difference indicates that the results of our best-fit $\text{Ly}\alpha$ EW scale lengths does not highly depend on the image depths and the detection incompleteness. In Section 6.1, we discuss the redshift evolution of the $\text{Ly}\alpha$ EW scale lengths.

We investigate LEW LAEs whose intrinsic $\text{Ly}\alpha$ EW value, $EW_{0,\text{Ly}\alpha}^{\text{int}}$, exceeds 240 \AA (e.g., Malhotra & Rhoads 2002; Dawson et al. 2004). To obtain $EW_{0,\text{Ly}\alpha}^{\text{int}}$, we correct for the

IGM attenuation for $\text{Ly}\alpha$ using the prescriptions of Madau (1995). In the HSC LAE ALL sample, we find that 45 and 230 LAEs have a LEW of $EW_{0,\text{Ly}\alpha}^{\text{int}} > 240 \text{ \AA}$, for $z \simeq 6.6$ and $z \simeq 5.7$ LAEs, respectively. These LEW LAEs are candidates of young-metal poor galaxies and AGNs. The fraction of the LEW LAEs in the sample is 21% for $z \simeq 5.7$ LAEs. The fraction of LEW LAEs at $z \simeq 5.7$ is comparable to that of previous studies on $z \simeq 5.7$ LAEs (e.g., $\simeq 25\%$ at $z \simeq 5.7$ in Ouchi et al. 2008; $\simeq 30 - 40\%$ at $z \simeq 5.7$ in Shimasaku et al. 2006). In contrast, the fraction of LEW LAEs at $z \simeq 6.6$ is 4% which is lower than that at $z \simeq 5.7$. The low fraction at $z \simeq 6.6$ might be due to the neutral hydrogen IGM absorbing the $\text{Ly}\alpha$ emission. Out of the LEW LAEs, 32 and 150 LAEs at $z \simeq 6.6$ and $z \simeq 5.7$ exceed $EW_{0,\text{Ly}\alpha}^{\text{int}} = 240$ beyond the 1σ uncertainty of $EW_{0,\text{Ly}\alpha}^{\text{int}}$,

Table 4. Properties of the LABs selected in the HSC NB Data.

Object ID	α (J2000)	δ (J2000)	NB_{tot} (mag)	UV_{tot} (mag)	$\log L_{\text{Ly}\alpha}$ (erg s^{-1})	$EW_{0,\text{Ly}\alpha}$ (\AA)	z_{spec}
(1)	(2)	(3)	(4)	(5)	(6)	(7)	(8)
<i>NB921</i> ($z \simeq 6.6$)							
HSC J100058+014815 ^a	10:00:58.00	+01:48:15.14	23.25	24.48	43.9 ^e	211 ± 20^e	6.604 ^a
HSC J021757–050844 ^b	02:17:57.58	–05:08:44.64	23.50	25.40	43.4 ^e	$78^{+8}_{-6}^e$	6.595 ^b
HSC J100334+024546 ^c	10:03:34.66	+02:45:46.56	23.61	24.97	43.5 ^e	61 ± 20^e	6.575 ^c
<i>NB816</i> ($z \simeq 5.7$)							
HSC J100129+014929	10:01:29.07	+01:49:29.81	23.47	25.87	43.4	95^{+40}_{-19}	5.707 ^d
HSC J100109+021513	10:01:09.72	+02:15:13.45	23.13	25.77	43.6	257^{+172}_{-76}	5.712 ^d
HSC J100123+015600	10:01:23.84	+01:56:00.46	23.94	26.43	43.3	106^{+70}_{-27}	5.726 ^d
HSC J095946+013208	09:59:46.73	+01:32:08.45	24.16	26.12	43.1	52^{+25}_{-13}	—
HSC J100139+015428	10:01:39.94	+01:54:28.34	24.11	26.58	43.2	100^{+66}_{-30}	—
HSC J161927+551144	16:19:27.73	+55:11:44.70	22.88	24.86	43.7	89^{+33}_{-20}	—
HSC J161403+535701	16:14:03.82	+53:57:01.25	23.53	25.32	43.4	51^{+23}_{-12}	—
HSC J232924+003600	23:29:24.85	+00:36:00.34	23.62	26.48	43.4	55^{+45}_{-14}	—

(1) Object ID.

(2) Right ascension.

(3) Declination.

(4) Total magnitudes of *NB921*- and *NB816*-bands for $z \simeq 6.6$ and $z \simeq 5.7$, respectively.(5) Total magnitudes of *y*- and *z*-bands for $z \simeq 6.6$ and $z \simeq 5.7$, respectively.(6) $\text{Ly}\alpha$ luminosity.(7) Rest-frame equivalent width of $\text{Ly}\alpha$ emission line.

(8) Spectroscopic redshift.

^a CR7 in Sobral et al. (2015).^b Himiko in Ouchi et al. (2009).^c Spectroscopically confirmed in Shibuya et al. (2017b).^d Spectroscopically confirmed in Mallery et al. (2012).^e Spectroscopic measurements from the literature.

respectively.

5.2 LABs at $z \simeq 5.7 - 6.6$

We search for LABs with spatially-extended $\text{Ly}\alpha$ emission. To identify LABs, we measure the NB isophotal areas, A_{iso} , for the forced LAEs. In this process, we include an unforced LAE, Himiko, which is an LAB identified in a previous SCam NB survey (Ouchi et al. 2009). First, we estimate the sky background level of the NB cutout images. Next, we run the SExtractor with the sky background level, and obtain the A_{iso} values as pixels with fluxes brighter than the 2σ sky fluctuation. Note that the NB magnitudes include both fluxes of $\text{Ly}\alpha$ and the rest-frame UV continuum emission. Instead of creating $\text{Ly}\alpha$ images by subtracting the flux contribution of the rest-frame UV continuum emission, we here simply use the NB images for consistency with previous studies (e.g., Ouchi et al. 2009).

Using A_{iso} and NB magnitude diagrams, we select LABs which are significantly extended compared to point sources. This selection is similar to that of Yang et al. (2010). Figure

8 presents A_{iso} as a function of total NB magnitude. We also plot star-like point sources which are randomly selected in HSC NB fields. The A_{iso} and NB magnitude selection window is defined by a 2.5σ deviation from the A_{iso} -NB magnitude distribution for the star-like point sources. The value of 2.5σ is applied for fair comparisons with previous studies of e.g., Yang et al. (2009) and Yang et al. (2010) who have used $\simeq 2 - 4\sigma$. We perform visual inspections for the NB cutout images to remove unreliable LABs which are significantly affected by e.g., diffuse halos of nearby bright stars.

In total, we identify 11 LABs at $z \simeq 5.7 - 6.6$. Figure 9 and Table 4 present multi-band cutout images and properties for the LABs, respectively. As shown in Figure 9, these LABs are spatially extended in NB. Our HSC LAB selection confirms that CR7 and Himiko have a spatially extended $\text{Ly}\alpha$ emission. Six out of our 11 LABs have been confirmed by our spectroscopic follow-up observations (Shibuya et al. 2017b) and previous studies (Ouchi et al. 2009; Mallery et al. 2012; Sobral et al. 2015). In Section 6.2, we discuss the redshift evolution of the LAB number density.

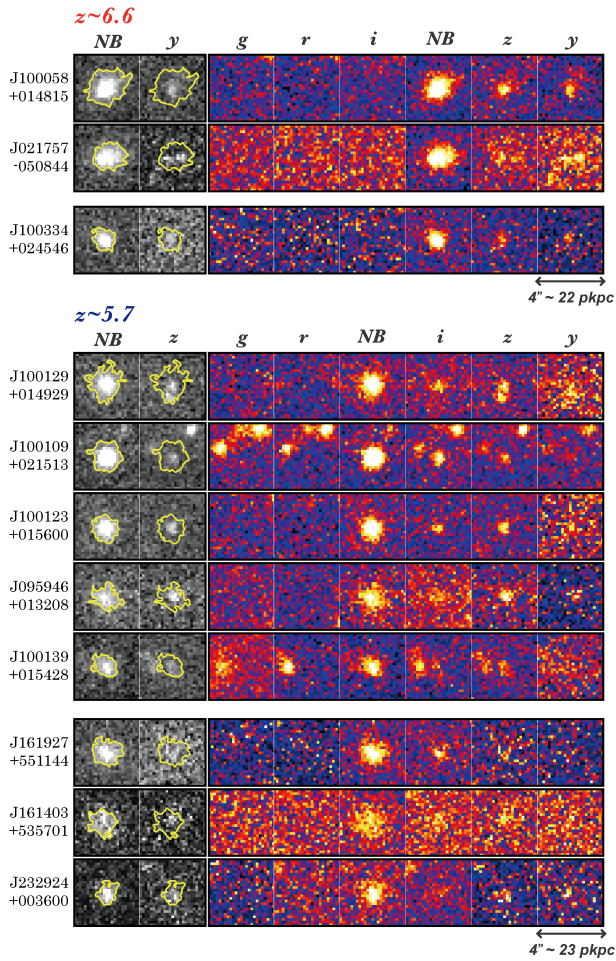


Fig. 9. Postage stamps of the LABs selected with the HSC NB data. The yellow contours indicate isophotal apertures with a threshold of 2σ sky background noise level. The size of the cutout images is $4'' \times 4''$.

Table 5. Best-fit Ly α EW Scale Lengths

Redshift	W_e (Å)	σ_g (Å)
(1)	(2)	(3)
6.6 (UD)	168^{+4}_{-4}	124^{+8}_{-8}
5.7 (UD)	138^{+6}_{-4}	164^{+2}_{-2}
6.6 (D)	140^{+14}_{-16}	154^{+4}_{-24}
5.7 (D)	168^{+18}_{-18}	128^{+36}_{-12}

(1) Redshift of the LAE sample. The parenthesis indicates the UD or D fields.
 (2) Best-fit Ly α EW scale length of the exponential form. (3) Best-fit Ly α EW scale length of the Gaussian form.

6 Discussion

6.1 Redshift Evolution of Ly α EW Distribution

We discuss the redshift evolution of the Ly α EW scale lengths in a compilation of the results from literature (Zheng et al. 2014; Ouchi et al. 2008; Nilsson et al. 2009; Hu et al. 2010;

Kashikawa et al. 2011; Cowie et al. 2011; Ciardullo et al. 2012). Figure 10 shows the redshift evolution of the Ly α EW scale lengths at $z \simeq 0 - 7$. Our best-fit Ly α scale lengths are comparable to that of Kashikawa et al. (2011) and/or Zheng et al. (2014) at $z \simeq 5.7 - 6.6$. The high Ly α EW scale lengths at high- z would indicate that metal-poor and/or less-dusty galaxies with a strong Ly α emission is more abundant at higher- z (e.g., Stark et al. 2011). In addition, Zheng et al. (2014) have found that the Ly α EW scale length increases towards high- z following a $(1+z)$ -form. Our W_e and σ_g values for $z \simeq 5.7 - 6.6$ are also roughly comparable to Zheng et al.'s $(1+z)$ -form evolution. However, no significant evolution in the Ly α EW scale lengths from $z \simeq 5.7$ to $z \simeq 6.6$ is identified in our HSC LAE data, although a possible decline in σ_g in the UD fields is found. A slight decrease both in W_e and σ_g from $z \simeq 5.7$ to $z \simeq 6.6$ has been found by Kashikawa et al. (2011). This sudden decline in the Ly α scale lengths at $z \simeq 6.6$ may be caused by the increasing hydrogen neutral fraction in the epoch of the cosmic reionization at $z \gtrsim 7$. Note that the Ly α EW scale length measurements would largely depend on BB and NB depths and Ly α EW cuts. Using deeper NB and BB images from the future HSC data release, we will examine the redshift evolution of Ly α scale lengths accurately.

6.2 Redshift Evolution of LAB Number Density

We discuss the redshift evolution of the LAB number density, N_{LAB} . Figure 11 shows N_{LAB} at $z \simeq 0 - 7$ measured by this study and the literature (Keel et al. 2009; Yang et al. 2009; Yang et al. 2010; Matsuda et al. 2009; Saito et al. 2006). For the plot of the N_{LAB} , Yang et al. (2010) have compiled N_{LAB} measurements down to an NB surface brightness (SB) limit of $5 \times 10^{-18} \text{ erg s}^{-1} \text{ cm}^{-2} \text{ arcsec}^{-2}$. The SB limits of our HSC NB data are $\simeq 5 \times 10^{-18}$ and $\simeq 8 \times 10^{-18} \text{ erg s}^{-1} \text{ cm}^{-2}$ for the UD and D fields, respectively. Our HSC NB images at least for the UD fields are comparably deep, allowing for fair comparisons with Yang et al.'s N_{LAB} plot. Our N_{LAB} values are 1.4×10^{-6} and $2.9 \times 10^{-7} \text{ Mpc}^{-3}$ (2.6×10^{-7} and $1.1 \times 10^{-7} \text{ Mpc}^{-3}$) at $z \simeq 5.7$ and $z \simeq 6.6$ in the UD (D) fields, respectively. The number density at $z \simeq 6 - 7$ is $\simeq 10 - 100$ times lower than those claimed for LABs at $z \simeq 2 - 3$ (e.g., Matsuda et al. 2004; Yang et al. 2009; Yang et al. 2010). As shown in Figure 11, there is an evolutionary trend that N_{LAB} increases from $z \simeq 7$ to $\simeq 3$ and subsequently decreases from $z \simeq 3$ to $\simeq 0$. This trend of the LAB number density evolution is similar to the Madau-Lilly plot of the cosmic SFR density (SFRD) evolution (e.g., Madau et al. 1996; Lilly et al. 1996). Similar to Shibuya et al. (2016), we fit the Madau-Lilly plot-type formula,

$$N_{\text{LAB}}(z) = a \times \frac{(1+z)^b}{1 + [(1+z)/c]^d}, \quad (6)$$

where a, b, c , and d are free parameters (Madau & Dickinson

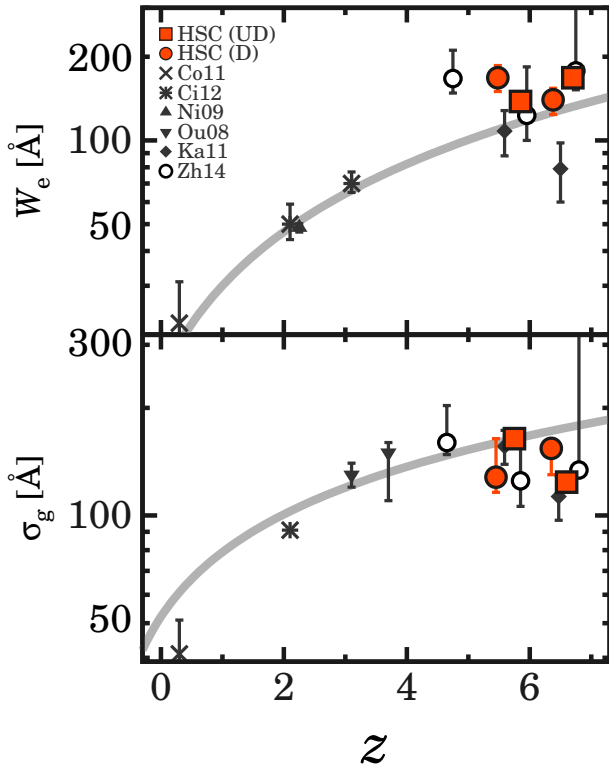


Fig. 10. Redshift evolution of the best-fit $\text{Ly}\alpha$ EW scale lengths of the exponential (top) and Gaussian (bottom) functions. The red squares and circles indicate our HSC LAEs in the UD and D fields, respectively. The black symbols are taken from the data points in literature which have been compiled in Zheng et al. (2014) (cross: Cowie et al. 2011; asterisks: Ciardullo et al. 2012; filled triangle: Nilsson et al. 2009; filled inverse triangles: Ouchi et al. 2008; filled diamonds: Kashikawa et al. 2011; open circles: results of Monte-Carlo simulations using data of Zheng et al. 2014 and Hu et al. 2010). The gray curves indicate the best-fit $(1+z)$ -form functions obtained in Zheng et al. (2014).

2014) to our N_{LAB} evolution. For the fitting, we exclude Matsuda et al. (2009)’s data point which has been obtained in a overdense region, SSA22. The best-fit parameters are $a = 9.1 \times 10^{-8}$, $b = 2.9$, $c = 5.0$, and $d = 11.7$.

The similarity of the cosmic SFRD and LAB evolution might indicate that the origin of LABs are related to the star formation activity. As described in Section 1, LABs are thought to be formed in physical mechanisms that are connected with the star formation, e.g., the cold gas accretion and the galactic superwinds. The cold gas accretion could produce the extended $\text{Ly}\alpha$ emission powered by the gravitational energy (e.g., Momose et al. 2016; Mas-Ribas & Dijkstra 2016; Mas-Ribas et al. 2017). On the other hand, the superwinds induced by the starbursts in the central galaxies would blow out the surrounding neutral gas, and form extended $\text{Ly}\alpha$ nebulae (e.g., Mori & Umemura 2006). The cold gas accretion rate and the strength of galactic superwinds are predicted to evolve with physical quantities related to the cosmic SFRD (e.g., Dekel et al. 2009; Kereš et al. 2009). The comparisons of the cosmic SFRD and LAB evolu-

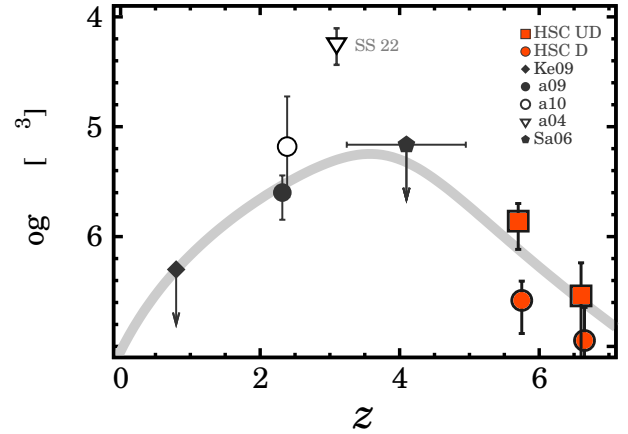


Fig. 11. Redshift evolution of the LAB number density. The filled red squares and filled red circles denote the LABs selected in the HSC UD and D fields, respectively. The error bars are given by Poisson statistics from the LAB number counts. The black symbols show LABs in the literature (filled diamond: Keel et al. 2009; filled circle: Yang et al. 2009; open circle: Yang et al. 2010; filled inverse-triangle: Matsuda et al. 2004; pentagon: Saito et al. 2006). All the measurements are based on LABs identified down to the surface brightness limit of $\simeq 5 \times 10^{-18} \text{ erg s}^{-1} \text{ cm}^{-2} \text{ arcsec}^{-2}$. The gray solid curve represents the best-fit formula of Equation 6 to the data points expect for the measurement in the SSA22 proto-cluster region.

tions would provide useful hints that LABs are formed in these scenarios.

However, it should be noted that the LAB selection method is not homogeneous in our comparison of N_{LAB} at $z \simeq 0 - 7$. There is a possibility that the N_{LAB} evolution from $z \simeq 7$ to $z \simeq 3$ is caused by the cosmological surface brightness dimming effect at high- z . The cosmological surface brightness dimming would significantly affect the detection and selection completeness for LABs at high- z . To confirm the N_{LAB} evolution and quantitatively compare with the cosmic SFRD, we need to homogenize the selection method for LABs at $z \simeq 2 - 7$ in the future HSC NB data.

7 Summary and Conclusions

We develop an unprecedentedly large catalog consisting of LAEs at $z = 5.7$ and 6.6 that are identified by the SILVERRUSH program with the first NB imaging data of the Subaru/HSC survey. The NB imaging data is about an order of magnitude larger than any other surveys for $z \simeq 6 - 7$ LAEs conducted to date.

Our findings are as follows:

- We identify 2,230 $\gtrsim L^*$ LAEs at $z = 5.7$ and 6.6 on the 13.8 and 21.2 deg^2 sky, respectively. We confirm that the LAE catalog is reliable on the basis of 96 LAEs whose spectroscopic redshifts are already determined by this program (Shibuya et al. 2017b) and the previous studies (e.g., Mallery et al. 2012). The LAE catalog is presented in this work, and published online.

- With the large LAE catalog, we derive the rest-frame Ly α EW distributions of LAEs at $z \simeq 5.7$ and $z \simeq 6.6$ that are reasonably explained by the exponential profile. The best-fit exponential (Gaussian) Ly α scale lengths are, on average of the UltraDeep and Deep fields, $153 \pm 18 \text{ \AA}$ and $154 \pm 15 \text{ \AA}$ ($146 \pm 24 \text{ \AA}$ and $139 \pm 14 \text{ \AA}$) at $z \simeq 5.7$ and $z \simeq 6.6$, respectively, showing no significant evolution from $z \simeq 5.7$ to $z \simeq 6.6$. We find 45 and 230 LAEs at $z \simeq 6.6$ and $z \simeq 5.7$ with a LEW of $EW_{0,\text{Ly}\alpha}^{\text{int}} > 240 \text{ \AA}$ corrected for the IGM attenuation for Ly α . The fraction of the LEW LAEs to all LAEs is $\simeq 4\%$ and $\simeq 21\%$ at $z \simeq 6.6$ and $z \simeq 5.7$, respectively. These LEW LAEs are candidates of young-metal poor galaxies and AGNs.
- We search for LABs that are LAEs with spatially extended Ly α emission whose profile is clearly distinguished from those of stellar objects at the $\gtrsim 3\sigma$ level. In the search, we identify 11 LABs in the HSC NB images down to a surface brightness limit of $\simeq 5 - 8 \times 10^{-18} \text{ erg s}^{-1} \text{ cm}^{-2}$ which is as deep as data of previous studies. The number density of the LABs at $z \simeq 6-7$ is $\sim 10^{-7} - 10^{-6} \text{ Mpc}^{-3}$ that is $\sim 10 - 100$ times lower than those claimed for LABs at $z \simeq 2 - 3$, suggestive of disappearing LABs at $z \gtrsim 6$, although the selection methods are different in the low and high- z LABs.

It should be noted that Ly α EW scale length derivation methods and the LAB selections are not homogeneous in a redshift range of $z \simeq 0 - 7$. Using the future $z \simeq 2.2, 5.7, 6.6$, and 7.3 HSC NB data, we will systematically investigate the redshift evolution of Ly α EW scale lengths and N_{LAB} at $z \simeq 2 - 7$ in homogeneous methods.

8 Appendix: Calculation of Ly α EW

In this section, we describe the method to calculate the $EW_{0,\text{Ly}\alpha}$ values. The procedures and the assumption of this method are similar to those of e.g., Malhotra & Rhoads (2002), Dawson et al. (2004), Gronwall et al. (2007), Kashikawa et al. (2011). For the calculation of $EW_{0,\text{Ly}\alpha}$, we assume that LAEs have a δ function-shaped Ly α line and the flat rest-frame UV continuum emission (i.e. $\beta_\nu = 0$, where β_ν is the UV spectral slope per unit frequency). In such an LAE spectrum, the magnitude, m , for a waveband filter with a transmission curve, T_ν , is described as follows:

$$48.6 + m = -2.5 \times \log_{10} \frac{\int_0^\infty (f_c + f_l \delta(\nu - \nu_\alpha)) T_\nu d\nu}{\int_0^\infty T_\nu d\nu}, \quad (7)$$

where f_l , f_c , $\delta(\nu)$, and ν_α is a Ly α line flux, the flux density of the rest-frame UV continuum emission, the δ function, and the observed frequency of Ly α , respectively. Here we also assume that the Ly α line is located at 9215 \AA (8177 \AA) which is the central wavelength of the NB921 (NB816) filter, for $z \simeq 6.6$ ($z \simeq 5.7$) LAEs. In this study, we do not take into account the IGM transmission for Ly α , if not specified. This is because

the IGM transmission for Ly α highly depends on the Ly α line velocity offset from the systemic redshift (e.g., Hashimoto et al. 2013; Shibuya et al. 2014b). The numerator of the logarithm in Equation (7) corresponds to

$$\begin{aligned} & f_c \int_{\nu_c}^\infty \exp(-\tau_{\text{eff}}) T_\nu d\nu + f_c \int_0^{\nu_c} T_\nu d\nu + f_l T_\nu(\nu_\alpha) \\ &= f_c B + f_c R + f_l T_\nu(\nu_\alpha). \end{aligned} \quad (8)$$

In Equation (8), we use B , R , and A that are defined by equations of

$$B \equiv \int_{\nu_c}^\infty \exp(-\tau_{\text{eff}}) T_\nu d\nu, \quad (9)$$

$$R \equiv \int_0^{\nu_c} T_\nu d\nu, \quad (10)$$

$$A \equiv \int_0^\infty T_\nu d\nu, \quad (11)$$

where τ_{eff} is the IGM optical depth calculated from analytical models of Madau (1995). Using Equations (7) and (8), we derive the flux density of the NB and BB filters, $\overline{f_{\text{NB}}}$ and $\overline{f_{\text{BB}}}$, as follows:

$$\overline{f_{\text{NB}}} = 10^{-0.4(m_{\text{NB}} + 48.6)} = \frac{f_c(B_{\text{NB}} + R_{\text{NB}}) + f_l T_{\text{NB}}(\nu_\alpha)}{A_{\text{NB}}}, \quad (12)$$

$$\overline{f_{\text{BB}}} = 10^{-0.4(m_{\text{BB}} + 48.6)} = \frac{f_c(B_{\text{BB}} + R_{\text{BB}})}{A_{\text{BB}}}. \quad (13)$$

The B , R , and A values with the subscripts of NB (BB) are calculated with the transmission curves of the NB (BB) filters, T_{NB} (T_{BB}). In this study, we use magnitudes of the y and z band filters which do not cover the wavelength of Ly α for $z \simeq 6.6$ and $z \simeq 5.7$ LAEs, respectively, indicating $T_{\text{BB}}(\nu_\alpha) = 0$. In the case that m_{BB} is fainter than the 1σ limit, we use the 1σ limiting magnitude for the $EW_{0,\text{Ly}\alpha}$ calculation. By combining the equations of $\overline{f_{\text{NB}}}$ and $\overline{f_{\text{BB}}}$, we obtain f_c and f_l ,

$$f_c = \frac{A_{\text{BB}} \overline{f_{\text{BB}}}}{B_{\text{BB}} + R_{\text{BB}}} = \overline{f_{\text{BB}}}, \quad (14)$$

$$f_l = \frac{A_{\text{NB}}(B_{\text{BB}} + R_{\text{BB}}) \overline{f_{\text{NB}}} - A_{\text{BB}}(B_{\text{NB}} + R_{\text{NB}}) \overline{f_{\text{BB}}}}{(B_{\text{BB}} + R_{\text{BB}}) T_{\text{NB}}(\nu_\alpha)} \quad (15)$$

$$= \frac{A_{\text{NB}} \overline{f_{\text{NB}}} - (B_{\text{NB}} + R_{\text{NB}}) \overline{f_{\text{BB}}}}{T_{\text{NB}}(\nu_\alpha)} \quad (16)$$

$$= a \times \overline{f_{\text{NB}}} - b \times \overline{f_{\text{BB}}}. \quad (17)$$

Note that $B_{\text{BB}} + R_{\text{BB}} = A_{\text{BB}}$ due to the negligible IGM absorption at the wavelengths of the BB filters. Here we define a and b as

$$a \equiv \frac{A_{\text{NB}}}{T_{\text{NB}}(\nu_\alpha)}, \quad (18)$$

$$b \equiv \frac{B_{\text{NB}} + R_{\text{NB}}}{T_{\text{NB}}(\nu_\alpha)}. \quad (19)$$

For the HSC *NB921* and *NB816* filters, the sets of the values are calculated to be $(a, b) \simeq (4.7, 2.3) \times 10^{12}$ and $(a, b) \simeq (5.2, 2.7) \times 10^{12}$, respectively. Using f_c and f_l , we calculate the $EW_{0, Ly\alpha}$ values via

$$EW_{0, Ly\alpha} = \frac{f_l}{f_c} \frac{c}{\nu^2} \frac{1}{1+z}. \quad (20)$$

To obtain the median values and uncertainties for $EW_{0, Ly\alpha}$, we perform Monte Carlo (MC) simulations in a method similar to that of e.g., Shimasaku et al. (2006). In the simulation, we randomly generate a flux density value, $\overline{f_{MC}}$, following a Gaussian probability distribution with an average of \overline{f} and a dispersion of the 1σ sky background noise, $\overline{f_{1\sigma}}$, for the NB and BB bands. Here we also randomize β_ν and ν_α in Gaussian probability distributions with 1σ dispersions of $\Delta\beta = 0.2$ and $\Delta\nu_\alpha = FWHM_{NB}/2.35$, respectively, where $FWHM_{NB}$ is the FWHM of the NB filters. The dispersion of $\Delta\beta = 0.2$ is typical for high- z galaxies (Bouwens et al. 2014). In the manner that are the same as described in this section, we calculate a $EW_{0, Ly\alpha}$ value using $\overline{f_{MC}}$ for NB and BB. In this process, negative values of f_c , f_l , and $EW_{0, Ly\alpha}$ are forced to be zero. Such a process is performed 1,000 times for each object. During the iteration, a simulated $EW_{0, Ly\alpha}$ value is discarded in the case that a $BB - NB$ color does not meet the selection criteria of Equations (1) and (2). Using the set of $EW_{0, Ly\alpha}$ values obtained from the MC simulations, we calculate the median values and the 16- and 84-percentile errors for $EW_{0, Ly\alpha}$.

Acknowledgments

We would like to thank James Bosch, Richard S. Ellis, Masao Hayashi, Robert H. Lupton, Michael A. Strauss for useful discussion and comments. We thank the anonymous referee for constructive comments and suggestions. This work is based on observations taken by the Subaru Telescope and the Keck telescope which are operated by the National Observatory of Japan. This work was supported by World Premier International Research Center Initiative (WPI Initiative), MEXT, Japan, KAKENHI (23244025) and (21244013) Grant-in-Aid for Scientific Research (A) through Japan Society for the Promotion of Science (JSPS), and an Advanced Leading Graduate Course for Photon Science grant. The NB816 filter was supported by Ehime University (PI: Y. Taniguchi). The NB921 filter was supported by KAKENHI (23244025) Grant-in-Aid for Scientific Research (A) through the Japan Society for the Promotion of Science (PI: M. Ouchi). NK is supported by the JSPS grant 15H03645. SY is supported by Faculty of Science, Mahidol University, Thailand and the Thailand Research Fund (TRF) through a research grant for new scholar (MRG5980153).

The Hyper Suprime-Cam (HSC) collaboration includes the astronomical communities of Japan and Taiwan, and Princeton University. The HSC instrumentation and software were developed by the National Astronomical Observatory of Japan (NAOJ), the Kavli Institute for the Physics and Mathematics of the Universe (Kavli IPMU), the University of Tokyo, the High Energy Accelerator Research Organization (KEK), the Academia Sinica Institute for Astronomy and Astrophysics in Taiwan (ASIAA), and Princeton University. Funding was contributed by the FIRST program from Japanese Cabinet Office, the Ministry of Education,

Culture, Sports, Science and Technology (MEXT), the Japan Society for the Promotion of Science (JSPS), Japan Science and Technology Agency (JST), the Toray Science Foundation, NAOJ, Kavli IPMU, KEK, ASIAA, and Princeton University.

This paper makes use of software developed for the Large Synoptic Survey Telescope. We thank the LSST Project for making their code available as free software at <http://dm.lsst.org>

The Pan-STARRS1 Surveys (PS1) have been made possible through contributions of the Institute for Astronomy, the University of Hawaii, the Pan-STARRS Project Office, the Max-Planck Society and its participating institutes, the Max Planck Institute for Astronomy, Heidelberg and the Max Planck Institute for Extraterrestrial Physics, Garching, The Johns Hopkins University, Durham University, the University of Edinburgh, Queen's University Belfast, the Harvard-Smithsonian Center for Astrophysics, the Las Cumbres Observatory Global Telescope Network Incorporated, the National Central University of Taiwan, the Space Telescope Science Institute, the National Aeronautics and Space Administration under Grant No. NNX08AR22G issued through the Planetary Science Division of the NASA Science Mission Directorate, the National Science Foundation under Grant No. AST-1238877, the University of Maryland, and Eotvos Lorand University (ELTE) and the Los Alamos National Laboratory.

Based on data collected at the Subaru Telescope and retrieved from the HSC data archive system, which is operated by Subaru Telescope and Astronomy Data Center at National Astronomical Observatory of Japan.

References

- Aihara, H., et al. 2017a, arXiv:1702.08449
- . 2017b, arXiv:1704.05858
- Ajiki, M., et al. 2002, *ApJL*, 576, L25
- Arrigoni Battaia, F., Hennawi, J. F., Prochaska, J. X., & Cantalupo, S. 2015a, *ApJ*, 809, 163
- Arrigoni Battaia, F., Yang, Y., Hennawi, J. F., Prochaska, J. X., Matsuda, Y., Yamada, T., & Hayashino, T. 2015b, *ApJ*, 804, 26
- Axelrod, T., Kantor, J., Lupton, R. H., & Pierfederici, F. 2010, An open source application framework for astronomical imaging pipelines
- Bertin, E., & Arnouts, S. 1996, *A&AS*, 117, 393
- Blanc, G. A., et al. 2011, *ApJ*, 736, 31
- Bond, N. A., Gawiser, E., Guaita, L., Padilla, N., Gronwall, C., Ciardullo, R., & Lai, K. 2012, *ApJ*, 753, 95
- Bosch, J., et al. 2017, ArXiv e-prints
- Bouwens, R. J., et al. 2014, *ApJ*, 793, 115
- Cai, Z., et al. 2017, *ApJ*, 837, 71
- Cantalupo, S., Arrigoni-Battaia, F., Prochaska, J. X., Hennawi, J. F., & Madau, P. 2014, *Nature*, 506, 63
- Cantalupo, S., Porciani, C., Lilly, S. J., & Miniati, F. 2005, *ApJ*, 628, 61
- Ciardullo, R., et al. 2012, *ApJ*, 744, 110
- Cowie, L. L., Barger, A. J., & Hu, E. M. 2010, *ApJ*, 711, 928
- Cowie, L. L., Hu, E. M., & Songaila, A. 2011, *ApJL*, 735, L38
- Dawson, S., et al. 2004, *ApJ*, 617, 707
- Dekel, A., et al. 2009, *Nature*, 457, 451
- Dressler, A., Martin, C. L., Henry, A., Sawicki, M., & McCarthy, P. 2011, *ApJ*, 740, 71
- Duval, F., Schaerer, D., Östlin, G., & Laursen, P. 2013, ArXiv e-prints
- Erb, D. K., Bogosavljević, M., & Steidel, C. C. 2011, *ApJL*, 740, L31
- Finkelstein, S. L., Rhoads, J. E., Malhotra, S., Grogin, N., & Wang, J. 2008, *ApJ*, 678, 655

- Finkelstein, S. L., Rhoads, J. E., Malhotra, S., Pirzkal, N., & Wang, J. 2007, *ApJ*, 660, 1023
- Gawiser, E., et al. 2007, *ApJ*, 671, 278
- Gronwall, C., et al. 2007, *ApJ*, 667, 79
- Guaita, L., et al. 2011, *ApJ*, 733, 114
- Haiman, Z., Abel, T., & Rees, M. J. 2000, *ApJ*, 534, 11
- Hansen, M., & Oh, S. P. 2006, *mnras*, 367, 979
- Harikane, Y., et al. 2017, arXiv:1704.06535
- Hashimoto, T., Ouchi, M., Shimasaku, K., Ono, Y., Nakajima, K., Rauch, M., Lee, J., & Okamura, S. 2013, *ApJ*, 765, 70
- Hashimoto, T., et al. 2017, *MNRAS*, 465, 1543
- Hayes, M., Scarlata, C., & Siana, B. 2011, *Nature*, 476, 304
- Hennawi, J. F., Prochaska, J. X., Cantalupo, S., & Arrigoni-Battaia, F. 2015, *Science*, 348, 779
- Hu, E. M., Cowie, L. L., Barger, A. J., Capak, P., Kakazu, Y., & Trouille, L. 2010, *ApJ*, 725, 394
- Ivezic, Z., et al. 2008, ArXiv e-prints
- Jurić, M., et al. 2015, ArXiv e-prints
- Kashikawa, N., et al. 2006, *ApJ*, 648, 7
- . 2011, *ApJ*, 734, 119
- . 2012, *ApJ*, 761, 85
- Kawanomoto, S. 2017, to be submitted to PASJ
- Keel, W. C., White, III, R. E., Chapman, S., & Windhorst, R. A. 2009, *AJ*, 138, 986
- Kereš, D., Katz, N., Fardal, M., Davé, R., & Weinberg, D. H. 2009, *MNRAS*, 395, 160
- Kodaira, K., et al. 2003, *PASJ*, 55, L17
- Kojima, T., Ouchi, M., Nakajima, K., Shibuya, T., Harikane, Y., & Ono, Y. 2016, ArXiv e-prints
- Konno, A., et al. 2014, *apj*, 797, 16
- . 2017, arXiv:1705.01222
- Kusakabe, H., Shimasaku, K., Nakajima, K., & Ouchi, M. 2015, *ApJL*, 800, L29
- Laursen, P., Duval, F., & Östlin, G. 2013, *ApJ*, 766, 124
- Laursen, P., & Sommer-Larsen, J. 2007, *ApJL*, 657, L69
- Laursen, P., Sommer-Larsen, J., & Andersen, A. C. 2009, *ApJ*, 704, 1640
- Lilly, S. J., Le Fevre, O., Hammer, F., & Crampton, D. 1996, *ApJL*, 460, L1
- Madau, P. 1995, *ApJ*, 441, 18
- Madau, P., & Dickinson, M. 2014, *ARA&A*, 52, 415
- Madau, P., Ferguson, H. C., Dickinson, M. E., Giavalisco, M., Steidel, C. C., & Fruchter, A. 1996, *MNRAS*, 283, 1388
- Magnier, E. A., et al. 2013, *ApJS*, 205, 20
- Malhotra, S., & Rhoads, J. E. 2002, *ApJL*, 565, L71
- . 2004, *ApJL*, 617, L5
- . 2006, *ApJL*, 647, L95
- Mallery, R. P., et al. 2012, *ApJ*, 760, 128
- Mas-Ribas, L., & Dijkstra, M. 2016, *ApJ*, 822, 84
- Mas-Ribas, L., Dijkstra, M., Hennawi, J. F., Trenti, M., Momose, R., & Ouchi, M. 2017, *ApJ*, 841, 19
- Matsuda, Y., et al. 2004, *AJ*, 128, 569
- . 2009, *MNRAS*, 400, L66
- . 2011, *MNRAS*, 410, L13
- Matthee, J., Sobral, D., Santos, S., Röttgering, H., Darvish, B., & Mobasher, B. 2015, *mnras*, 451, 400
- Momose, R., et al. 2016, *MNRAS*, 457, 2318
- Mori, M., & Umemura, M. 2006, *Nature*, 440, 644
- Murayama, T., et al. 2007, *ApJS*, 172, 523
- Nagao, T., et al. 2008, *ApJ*, 680, 100
- Nakajima, K., & Ouchi, M. 2014, *MNRAS*, 442, 900
- Nakajima, K., Ouchi, M., Shimasaku, K., Hashimoto, T., Ono, Y., & Lee, J. C. 2013, *ApJ*, 769, 3
- Nakajima, K., et al. 2012, *ApJ*, 745, 12
- Neufeld, D. A. 1991, *ApJL*, 370, L85
- Nilsson, K. K., Tapken, C., Möller, P., Freudling, W., Fynbo, J. P. U., Meisenheimer, K., Laursen, P., & Östlin, G. 2009, *A&A*, 498, 13
- Oke, J. B., & Gunn, J. E. 1983, *ApJ*, 266, 713
- Ono, Y., et al. 2010, *MNRAS*, 402, 1580
- . 2017, arXiv:1704.06004
- Ota, K., et al. 2017, ArXiv e-prints
- Ouchi, M., et al. 2008, *ApJs*, 176, 301
- . 2009, *ApJ*, 696, 1164
- . 2010, *ApJ*, 723, 869
- . 2017, arXiv:1704.07455
- Oyarzún, G. A., et al. 2016, *ApJL*, 821, L14
- Planck Collaboration et al. 2016, *A&A*, 594, A13
- Prescott, M. K. M., Dey, A., & Jannuzi, B. T. 2009, *ApJ*, 702, 554
- . 2012a, *ApJ*, 748, 125
- . 2013, *ApJ*, 762, 38
- Prescott, M. K. M., Martin, C. L., & Dey, A. 2015, *ApJ*, 799, 62
- Prescott, M. K. M., et al. 2012b, *ApJ*, 752, 86
- Rhoads, J. E., & Malhotra, S. 2001, *ApJL*, 563, L5
- Saito, T., Shimasaku, K., Okamura, S., Ouchi, M., Akiyama, M., & Yoshida, M. 2006, *ApJ*, 648, 54
- Salpeter, E. E. 1955, *ApJ*, 121, 161
- Schlaflly, E. F., et al. 2012, *ApJ*, 756, 158
- Shibuya, T., Kashikawa, N., Ota, K., Iye, M., Ouchi, M., Furusawa, H., Shimasaku, K., & Hattori, T. 2012, *ApJ*, 752, 114
- Shibuya, T., Ouchi, M., Kubo, M., & Harikane, Y. 2016, *ApJ*, 821, 72
- Shibuya, T., Ouchi, M., Nakajima, K., Yuma, S., Hashimoto, T., Shimasaku, K., Mori, M., & Umemura, M. 2014a, ArXiv e-prints
- Shibuya, T., et al. 2014b, *apj*, 788, 74
- . 2017b, to be submitted to PASJ
- Shimasaku, K., et al. 2006, *PASJ*, 58, 313
- Sobral, D., Matthee, J., Darvish, B., Schaerer, D., Mobasher, B., Röttgering, H. J. A., Santos, S., & Hemmati, S. 2015, *apj*, 808, 139
- Stark, D. P., Ellis, R. S., & Ouchi, M. 2011, *ApJL*, 728, L2+
- Steidel, C. C., Adelberger, K. L., Shapley, A. E., Pettini, M., Dickinson, M., & Giavalisco, M. 2000, *ApJ*, 532, 170
- Taniguchi, Y., & Shioya, Y. 2000, *ApJL*, 532, L13
- Taniguchi, Y., et al. 2005, *PASJ*, 57, 165
- . 2009, *ApJ*, 701, 915
- Tonry, J. L., et al. 2012, *ApJ*, 750, 99
- Toshikawa, J., et al. 2017, ArXiv e-prints
- Yajima, H., Li, Y., & Zhu, Q. 2013, *ApJ*, 773, 151
- Yajima, H., Li, Y., Zhu, Q., Abel, T., Gronwall, C., & Ciardullo, R. 2012, ArXiv e-prints
- Yang, Y., Zabludoff, A., Eisenstein, D., & Davé, R. 2010, *ApJ*, 719, 1654
- Yang, Y., Zabludoff, A., Tremonti, C., Eisenstein, D., & Davé, R. 2009, *ApJ*, 693, 1579
- Zheng, Z., Cen, R., Trac, H., & Miralda-Escudé, J. 2010, *ApJ*, 716, 574
- Zheng, Z., & Wallace, J. 2013, ArXiv e-prints
- Zheng, Z.-Y., Wang, J.-X., Malhotra, S., Rhoads, J. E., Finkelstein, S. L., & Finkelstein, K. 2014, *MNRAS*, 439, 1101
- Zheng, Z.-Y., et al. 2017, ArXiv e-prints